Journal of
Ceramic Science
and Technology

J. Ceram. Sci. Technol., 09 [4] 435-464 (2018)
DOI: 10.4416/JCST2018-00049
available online at: http://www.ceramic-science.com

Synergistic Effects of Loading Sequences and Phase Angles on Thermomechanical Fatigue Damage Evolution of Silicon-Carbide-Fiber-Reinforced Ceramic-Matrix Composites

L. Li*

College of Civil Aviation, Nanjing University of Aeronautics and Astronautics, No.29 Yudao St., Nanjing 210016, PR China

received August 28, 2018; received in revised form September 10, 2018; accepted October 15, 2018

Abstract

In this paper, the synergistic effects of loading sequences and phase angles on the thermomechanical fatigue (TMF) damage evolution of silicon-carbide-fiber-reinforced ceramic-matrix composites (SiC–CMCs) are investigated. Mechanisms-based micromechanical TMF damage models using the hysteresis-based damage parameters are developed to describe the internal damage development of fiber-reinforced CMCs. Relationships between the damage evolution (i.e. TMF hysteresis dissipated energy, hysteresis modulus and peak strain), loading sequences (i.e. constant peak stress loading, low–high peak stress loading sequence and high–low peak stress loading sequence), phase angles (i.e. $\theta = 0$, $\pi/3$, $\pi/2$ and π) and micro damage states (i.e. fiber/matrix interface debonding/sliding and fiber/matrix interface debonding ratio) are established. The effects of fiber volume fraction, matrix crack spacing, fiber/matrix interface debonded energy, stress ratio and thermal cyclic temperature range on the damage evolution of SiC/SiC composite for different loading sequences (i.e. constant peak stress loading, low–high peak stress loading sequence and high–low peak stress loading sequence) are analyzed. The experimental and theoretical in-phase thermomechanical fatigue damage evolution of SiC/SiC and SiC/magnesium aluminosilicate (MAS) composite subjected to different loading sequences is predicted.

Keywords: Ceramic-matrix composites (CMCs), thermomechanical fatigue (TMF), damage evolution, phase angle, loading sequence

I. Introduction

The development of high-temperature materials over the past 40 years has been one of the key factors responsible for improvements in the performance of gas turbines. Ceramics are refractory materials and attractive for gas turbine applications. Monolithic ceramics have been around for over 40 years but have not found applications in gas turbines as they do not have adequate damage tolerance and fail catastrophically. Fiber-reinforced ceramic-matrix composites (CMCs) are damage-tolerant, tough, lightweight and capable of withstanding temperatures 533,15 K hotter than nickel (Ni) superalloys can endure. Replacing superalloys with CMCs would permit the gas temperature to be increased, the cooling requirement to be suppressed and limited, the efficiency of the engine to be increased, and both the weight and the noise/pollution level to be reduced [1–3]. The LEAP aircraft engine, manufactured by CFM International, became the first widely developed CMCs-containing product in 2016. The LEAP engine has a turbine shroud lining its hottest zone, so it can operate at up to 1588,71 K. Fiber-reinforced CMCs need less cooling air than nickel-based superalloys and are part of a suite of technologies that contribute to 15-% fuel savings for LEAP compared to its predecessor, the CFM 56 engine[4].

Under thermomechanical fatigue (TMF) loading, the mechanical behavior of fiber-reinforced CMCs involves cycling loads and cycling temperature [5, 6 and 7]. The cyclic fatigue stress and repetitive temperature can change the stress and temperature field, and cause serious physical and chemical damage inside composites, i.e. matrix multicracking [8], fiber/matrix interface debonding/sliding [9], fiber/matrix interphase oxidation and fibers fracture [10]. Burr *et al.* [11] proposed a constitutive law for CMCs considering multiple damage mechanisms, which induce loss of stiffness, inelastic strain, creep strain, hysteresis loops, and crack closure. Based on a combination of the continuum damage mechanics (CDM) with micromechanical models, the monotonic, cycling and creep loading of CMCs were analyzed. Mei *et al.* [12] compared the mechanical response of two- and three-dimensional C/SiC composites subjected to thermal cycling and mechanical fatigue in an oxidizing atmosphere. Compared with 2D architecture, the braided 3D C/SiC composites exhibit higher retained strength after 50 thermal cycles, and better damage resistance against oxidation and thermal shock. Foringer *et al.* [13] developed a micromech-

* Corresponding author: llb451@nuaa.edu.cn

anistic-based approach to fatigue life modeling of titanium-based metal-matrix composites (MMCs). The life-fraction fatigue model involved the linear summation of damage from the fiber and the matrix constituents of the composite. The fatigue lives of unidirectional, cross-ply and quasi-isotropic MMCs for different loading conditions, i.e. isothermal fatigue, in-phase (IP) and out-of-phase (OP) TMF, were predicted. Gocmez *et al.* [14] developed a new multiaxial low cycle fatigue criterion based on the dissipated plastic strain energy for cast iron in isothermal and thermomechanical out-of-phase loading. The nondestructive techniques (NDT), i.e. infrared thermography [15], acoustic emission [16, 17 and 18] and electrical resistivity [19], have been proposed to monitor the damage evolution in fiber-reinforced CMCs. However, these NDT methods cannot be applied for damage monitoring at elevated temperature above 1000 °C. Energy dissipation under cyclic loading can be used to monitor the internal damage in fiber-reinforced CMCs [20, 21, 22 and 23]. Under multiple loading sequence, the low–high loading sequence and high–low loading sequence affect the matrix cracking and fiber/matrix interface debonding/sliding, and the internal damage of fiber-reinforced CMCs [24]. Li [25, 26] investigated the fatigue damage behavior of unidirectional CMCs under multiple loading sequence at room temperature. Under TMF loading, the thermal cyclic temperature affects the fiber/matrix interface shear stress upon unloading and reloading, and with increasing applied cycle number, the fiber/matrix interface shear stress also degrades owing to the fiber/matrix interface wear [27–29]. However, considering the coupling effects of multiple loading sequence, thermal cyclic temperature, and applied cycle number, the synergistic effects of loading sequence and phase angle on the damage evolution of fiber-reinforced CMCs have not been investigated.

The objective of this paper is to investigate the synergistic effects of loading sequence and phase angle on the damage evolution of SiC-fiber-reinforced CMCs. Mechanisms-based micromechanical TMF damage models using the hysteresis-based damage parameters are developed to describe the internal damage development of fiber-reinforced CMCs. The relationships between the damage evolution (i.e. TMF hysteresis dissipated energy, hysteresis modulus and peak strain), loading sequences (i.e. constant peak stress loading, low–high peak stress loading sequence and high–low peak stress loading sequence), phase angles (i.e. θ= 0, π/3, π/2 and π) and micro damage states (i.e. fiber/matrix interface debonding/sliding and fiber/matrix interface debonding ratio) are established. The effects of fiber volume fraction, matrix crack spacing, fiber/matrix interface debonded energy, stress ratio and thermal cyclic temperature range on the damage evolution of SiC/SiC composite for different loading sequences (i.e. constant peak stress loading, low–high peak stress loading sequence and high–low peak stress loading sequence) are analyzed. The experimental and theoretical in-phase thermomechanical fatigue damage evolution of SiC/SiC and SiC/MAS composite subjected to different loading sequences is predicted.

II. Theoretical Analysis

Under TMF loading, the thermal cyclic temperature changes with decreasing or increasing applied stress upon unloading or reloading. The variation of temperature and loading sequence with increasing applied cycles can be divided into four different cases, as shown in Fig. 1, including:

(1) Case 1, in-phase thermomechanical fatigue loading with $\theta = 0$;
(2) Case 2, out-of-phase thermomechanical fatigue loading with $\theta = \pi/3$;
(3) Case 3, out-of-phase thermomechanical fatigue loading with $\theta = \pi/2$;
(4) Case 4, out-of-phase thermomechanical fatigue loading with $\theta = \pi$.

For each phase angle, three loading cases are considered, as follows:

(1) Case 1, constant fatigue peak stress loading;
(2) Case 2, low–high peak stress loading sequence;
(3) Case 3, hig–low peak stress loading sequence.

Under multiple loading sequence, the cyclic and temperature-dependent fiber/matrix interface shear stress can be described using the following equation [30]:

$$\tau_{\mathrm{i}}(T,N) = \tau_0(N) + \mu \frac{|\alpha_{\mathrm{rf}} - \alpha_{\mathrm{rm}}|(T_0 - T)}{A} \tag{1}$$

where μ denotes the interfacial frictional coefficient [31, 32]; a_{rf} and a_{rm} denote the fiber and matrix radial thermal expansion coefficient, respectively; A is a constant depending on the elastic properties of the matrix and fibers; and $\tau_0(N)$ denotes the applied cyclic-dependent interface shear stress [33]

$$\left(\tau_{\mathrm{initial}} - \tau_{\mathrm{steady}}\right) / \left(\tau_0(N) - \tau_{\mathrm{steady}}\right) = (1+b_0)\left(1+b_0 N^j\right)^{-1} \tag{2}$$

where τ_{initial} denotes the fiber/matrix interface shear stress at the first applied cycle; τ_{steady} denotes the final fiber/matrix interface shear stress; b_0 is a coefficient; and j is an exponent that determines the rate at which interface shear stress drops with the number of cycles N.

(1) Stress analysis

Upon first loading to the fatigue peak stress of $\sigma_{\max 1}$, it is assumed that matrix multiple cracking and fiber/matrix interface debonding occur. After experiencing N_1 cycles, the fiber/matrix interface shear stress $\tau_0(N)$ in the interface debonded region degrades owing to interface wear and/or interface oxidation. When the fatigue peak stress increases from $\sigma_{\max 1}$ to $\sigma_{\max 2}$, the fiber/matrix interface debonded length continues to propagate along the fiber/matrix interface. The shear-lag model is adopted to analyze the stress distribution in the interface wear region, new interface debonded region and interface bonded region.

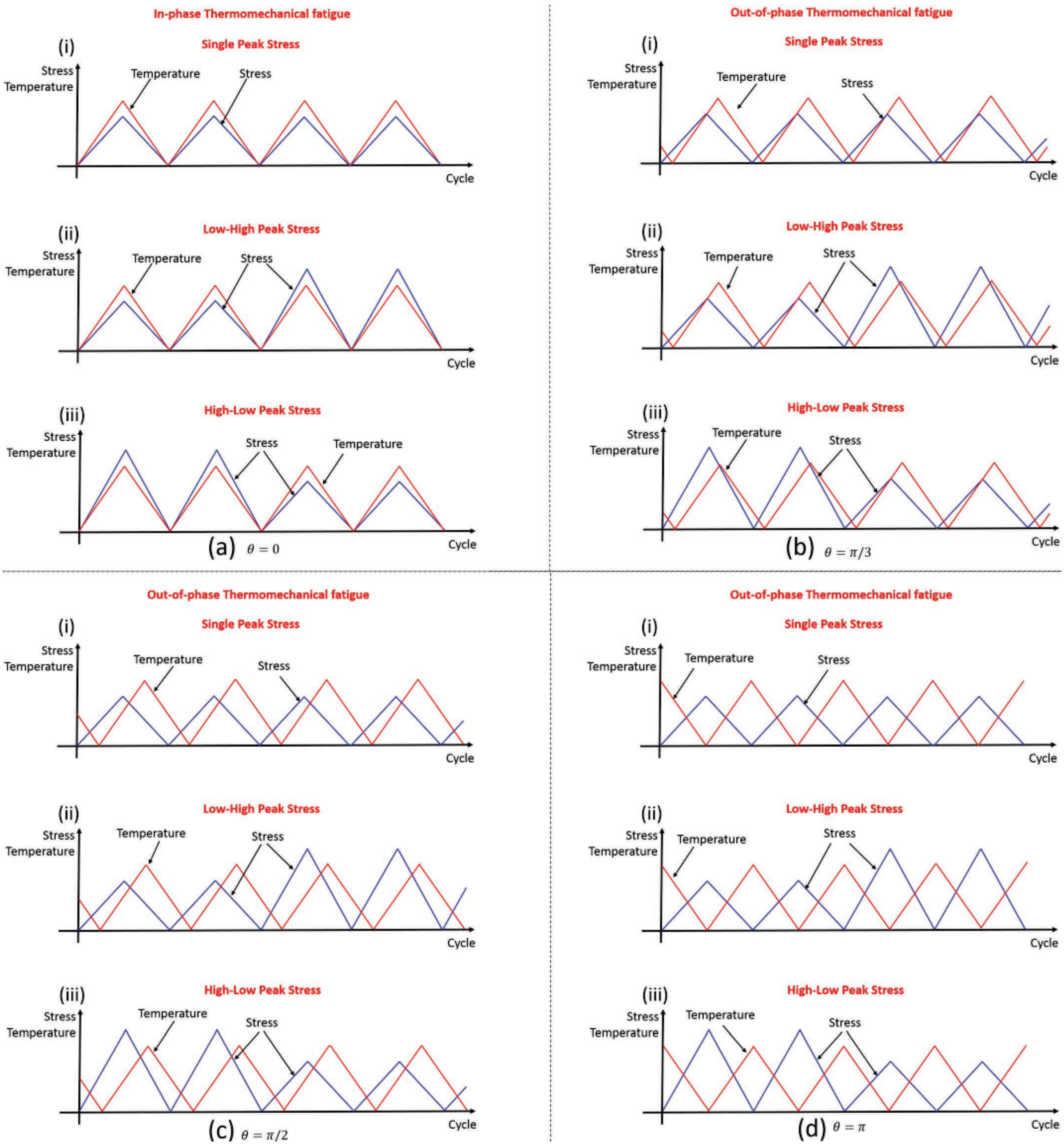

Fig. 1: The schematic of thermomechanical fatigue loading under single and low-high/high-low multiple loading sequence and different phase angles of (a) $\theta = 0$; (b) $\theta = \pi/3$; (c) $\theta = \pi/2$; and (d) $\theta = \pi$.

$$\sigma_{\mathrm{f}}(x) = \begin{cases} \dfrac{\sigma}{V_{\mathrm{f}}} - \dfrac{2\tau_{\mathrm{i}}(T, N_1)}{r_{\mathrm{f}}} x, x \in (0, \xi) \\ \dfrac{\sigma}{V_{\mathrm{f}}} - \dfrac{2\tau_{\mathrm{i}}(T, N_1)}{r_{\mathrm{f}}} \xi - \dfrac{2\tau_{\mathrm{i}}(T, N - N_1)}{r_{\mathrm{f}}} (x - \xi), x \in (\xi, l_{\mathrm{d}}) \\ \sigma_{\mathrm{fo}} + \left[\dfrac{V_{\mathrm{m}}}{V_{\mathrm{f}}} \sigma_{\mathrm{mo}} - 2\dfrac{\tau_{\mathrm{i}}(T, N_1)}{r_{\mathrm{f}}} \xi - 2\dfrac{\tau_{\mathrm{i}}(T, N - N_1)}{r_{\mathrm{f}}} (l_{\mathrm{d}} - \xi) \right] \exp\left(-\rho \dfrac{x - l_{\mathrm{d}}}{r_{\mathrm{f}}} \right), x \in \left(l_{\mathrm{d}}, \dfrac{l_{\mathrm{c}}}{2} \right) \end{cases} \tag{3}$$

$$\sigma_{\mathrm{f}}(x)=\begin{cases}\dfrac{\sigma}{V_{\mathrm{f}}}-\dfrac{2\tau_{\mathrm{i}}(T,N_1)}{r_{\mathrm{f}}}x, x\in(0,\xi)\\ \dfrac{\sigma}{V_{\mathrm{f}}}-\dfrac{2\tau_{\mathrm{i}}(T,N_1)}{r_{\mathrm{f}}}\xi-\dfrac{2\tau_{\mathrm{i}}(T,N-N_1)}{r_{\mathrm{f}}}(x-\xi), x\in(\xi,l_{\mathrm{d}})\\ \sigma_{\mathrm{fo}}+\left[\dfrac{V_{\mathrm{m}}}{V_{\mathrm{f}}}\sigma_{\mathrm{mo}}-2\dfrac{\tau_{\mathrm{i}}(T,N_1)}{r_{\mathrm{f}}}\xi-2\dfrac{\tau_{\mathrm{i}}(T,N-N_1)}{r_{\mathrm{f}}}(l_{\mathrm{d}}-\xi)\right]\exp\left(-\rho\dfrac{x-l_{\mathrm{d}}}{r_{\mathrm{f}}}\right), x\in\left(l_{\mathrm{d}},\dfrac{l_{\mathrm{c}}}{2}\right)\end{cases} \tag{4}$$

$$\tau_{\mathrm{i}}(x)=\begin{cases}\tau_{\mathrm{i}}(T,N_1), x\in(0,\xi)\\ \tau_{\mathrm{i}}(T,N-N_1), x\in(\xi,l_{\mathrm{d}})\\ \dfrac{\rho}{2}\left[\dfrac{V_{\mathrm{m}}}{V_{\mathrm{f}}}\sigma_{\mathrm{mo}}-2\dfrac{\tau_{\mathrm{i}}(T,N_1)}{r_{\mathrm{f}}}\xi-\dfrac{2\tau_{\mathrm{i}}(T,N-N_1)}{r_{\mathrm{f}}}(l_{\mathrm{d}}-\xi)\right]\exp\left(-\rho\dfrac{x-l_{\mathrm{d}}}{r_{\mathrm{f}}}\right), x\in\left(l_{\mathrm{d}},\dfrac{l_{\mathrm{c}}}{2}\right)\end{cases} \tag{5}$$

where V_{f} and V_{m} denote the fiber and matrix volume fraction, respectively; r_{f} denotes the fiber radius; ξ denotes the interface wear length; l_{d} denotes the fiber/matrix interface debonded length; l_{c} denotes the matrix crack spacing; σ_{fo} and σ_{mo} denote the fiber and matrix stress in the bonded region, respectively; ρ denotes the BHE shear-lag model parameter [34].

Upon unloading from the fatigue peak stress of $\sigma_{\max 2}$, the interface-debonded region can be divided into three regions, i.e. the interface counter-slip region with the interface shear stress of $\tau_{\mathrm{i}}(T, N_1)$, the interface counter-slip region with the interface shear stress of $\tau_{\mathrm{i}}(T, N-N_1)$, and the interface slip region with the interface shear stress of $\tau_{\mathrm{i}}(T, N-N_1)$. The micro stress distributions in the interface counter-slip region, interface slip region and interface bonded region upon unloading are determined with the following equations:

$$\begin{cases}\sigma_{\mathrm{f}}(x)=\dfrac{\sigma}{V_{\mathrm{f}}}+\dfrac{2\tau_{\mathrm{i}}(T,N_1)}{r_{\mathrm{f}}}x, x\in(0,\xi)\\ \sigma_{\mathrm{f}}(x)=\dfrac{\sigma}{V_{\mathrm{f}}}+\dfrac{2\tau_{\mathrm{i}}(T,N_1)}{r_{\mathrm{f}}}\xi+\dfrac{2\tau_{\mathrm{i}}(T,N-N_1)}{r_{\mathrm{f}}}(x-\xi), x\in(\xi,y)\\ \sigma_{\mathrm{f}}(x)=\dfrac{\sigma}{V_{\mathrm{f}}}+\dfrac{2\tau_{\mathrm{i}}(T,N_1)}{r_{\mathrm{f}}}\xi+\dfrac{2\tau_{\mathrm{i}}(T,N-N_1)}{r_{\mathrm{f}}}(2y-\xi-x), x\in(y,l_{\mathrm{d}})\\ \sigma_{\mathrm{f}}(x)=\sigma_{\mathrm{fo}}+\left[\dfrac{V_{\mathrm{m}}}{V_{\mathrm{f}}}\sigma_{\mathrm{mo}}+\dfrac{2\tau_{\mathrm{i}}(T,N_1)}{r_{\mathrm{f}}}\xi+\dfrac{2\tau_{\mathrm{i}}(T,N-N_1)}{r_{\mathrm{f}}}(2y-\xi-l_{\mathrm{d}})\right]\exp\left(-\rho\dfrac{x-l_{\mathrm{d}}}{r_{\mathrm{f}}}\right), x\in\left(l_{\mathrm{d}},\dfrac{l_{\mathrm{c}}}{2}\right)\end{cases} \tag{6}$$

$$\begin{cases}\sigma_{\mathrm{m}}(x)=-2\dfrac{V_{\mathrm{f}}}{V_{\mathrm{m}}}\dfrac{\tau_{\mathrm{i}}(T,N_1)}{r_{\mathrm{f}}}x, x\in(0,\xi)\\ \sigma_{\mathrm{m}}(x)=-2\dfrac{V_{\mathrm{f}}}{V_{\mathrm{m}}}\dfrac{\tau_{\mathrm{i}}(T,N_1)}{r_{\mathrm{f}}}\xi-2\dfrac{V_{\mathrm{f}}}{V_{\mathrm{m}}}\dfrac{\tau_{\mathrm{i}}(T,N-N_1)}{r_{\mathrm{f}}}(x-\xi), x\in(\xi,y)\\ \sigma_{\mathrm{m}}(x)=-2\dfrac{V_{\mathrm{f}}}{V_{\mathrm{m}}}\dfrac{\tau_{\mathrm{i}}(T,N_1)}{r_{\mathrm{f}}}\xi-2\dfrac{V_{\mathrm{f}}}{V_{\mathrm{m}}}\dfrac{\tau_{\mathrm{i}}(T,N-N_1)}{r_{\mathrm{f}}}(2y-\xi-x), x\in(\xi,l_{\mathrm{d}})\\ \sigma_{\mathrm{m}}(x)=\sigma_{\mathrm{mo}}-\left[\sigma_{\mathrm{mo}}+2\dfrac{V_{\mathrm{f}}}{V_{\mathrm{m}}}\dfrac{\tau_{\mathrm{i}}(T,N_1)}{r_{\mathrm{f}}}\xi+2\dfrac{V_{\mathrm{f}}}{V_{\mathrm{m}}}\dfrac{\tau_{\mathrm{i}}(T,N-N_1)}{r_{\mathrm{f}}}(2y-\xi-l_{\mathrm{d}})\right]\exp\left(-\rho\dfrac{x-l_{\mathrm{d}}}{r_{\mathrm{f}}}\right), x\in\left(l_{\mathrm{d}},\dfrac{l_{\mathrm{c}}}{2}\right)\end{cases} \tag{7}$$

$$\begin{cases}\tau_{\mathrm{i}}(x)=-\tau_{\mathrm{i}}(T,N_1), x\in(0,\xi)\\ \tau_{\mathrm{i}}(x)=-\tau_{\mathrm{i}}(T,N-N_1), x\in(\xi,y)\\ \tau_{\mathrm{i}}(x)=\tau_{\mathrm{i}}(T,N-N_1), x\in(y,l_{\mathrm{d}})\\ \tau_{\mathrm{i}}(x)=\dfrac{\rho}{2}\left[\dfrac{V_{\mathrm{m}}}{V_{\mathrm{f}}}\sigma_{\mathrm{mo}}+\dfrac{2\tau_{\mathrm{i}}(T,N_1)}{r_{\mathrm{f}}}\xi+\dfrac{2\tau_{\mathrm{i}}(T,N-N_1)}{r_{\mathrm{f}}}(2y-\xi-l_{\mathrm{d}})\right]\exp\left(-\rho\dfrac{x-l_{\mathrm{d}}}{r_{\mathrm{f}}}\right), x\in\left(l_{\mathrm{d}},\dfrac{l_{\mathrm{c}}}{2}\right)\end{cases} \tag{8}$$

where y denotes the fiber/matrix interface counter-slip length.

Upon reloading to the fatigue peak stress of $\sigma_{\max 2}$, the fiber/matrix interface debonded length can be divided into four regions, i.e. the interface new-slip region with the interface shear stress of $\tau_{\mathrm{i}}(T, N_1)$, the interface counter-slip region with the interface shear stress of $\tau_{\mathrm{i}}(T, N_1)$, the interface counter-slip region with the interface shear stress of $\tau_{\mathrm{i}}(T, N-N_1)$, and the interface slip region with the interface shear stress of $\tau_{\mathrm{i}}(T, N-N_1)$. The micro stress distributions in the interface new-slip region, interface counter-slip region, interface slip region and interface-bonded region upon reloading are determined with the following equations:

$$\begin{cases} \sigma_{\mathrm{f}}(x) = \dfrac{\sigma}{V_{\mathrm{f}}} - \dfrac{2\tau_{\mathrm{i}}(T,N_1)}{r_{\mathrm{f}}}x, x \in (0,z) \\ \sigma_{\mathrm{f}}(x) = \dfrac{\sigma}{V_{\mathrm{f}}} - \dfrac{2\tau_{\mathrm{i}}(T,N_1)}{r_{\mathrm{f}}}(2z-x), x \in (z,\xi) \\ \sigma_{\mathrm{f}}(x) = \dfrac{\sigma}{V_{\mathrm{f}}} - \dfrac{2\tau_{\mathrm{i}}(T,N_1)}{r_{\mathrm{f}}}(2z-\xi) + \dfrac{2\tau_{\mathrm{i}}(T,N-N_1)}{r_{\mathrm{f}}}(x-\xi), x \in (\xi,y) \\ \sigma_{\mathrm{f}}(x) = \dfrac{\sigma}{V_{\mathrm{f}}} - \dfrac{2\tau_{\mathrm{i}}(T,N_1)}{r_{\mathrm{f}}}(2z-\xi) + \dfrac{2\tau_{\mathrm{i}}(T,N-N_1)}{r_{\mathrm{f}}}(2y-\xi-x), x \in (y,l_{\mathrm{d}}) \\ \sigma_{\mathrm{f}}(x) = \sigma_{\mathrm{fo}} + \left[\dfrac{V_{\mathrm{m}}}{V_{\mathrm{f}}}\sigma_{\mathrm{mo}} - \dfrac{2\tau_{\mathrm{i}}(T,N_1)}{r_{\mathrm{f}}}(2z-\xi) + \dfrac{2\tau_{\mathrm{i}}(T,N-N_1)}{r_{\mathrm{f}}}(2y-\xi-l_{\mathrm{d}})\right]\exp\left(-\rho\dfrac{x-l_{\mathrm{d}}}{r_{\mathrm{f}}}\right), x \in \left(l_{\mathrm{d}}, \dfrac{l_{\mathrm{c}}}{2}\right) \end{cases} \tag{9}$$

$$\begin{cases} \sigma_{\mathrm{m}}(x) = 2\dfrac{V_{\mathrm{f}}}{V_{\mathrm{m}}}\dfrac{\tau_{\mathrm{i}}(T,N_1)}{r_{\mathrm{f}}}x, x \in (0,z) \\ \sigma_{\mathrm{m}}(x) = 2\dfrac{V_{\mathrm{f}}}{V_{\mathrm{m}}}\dfrac{\tau_{\mathrm{i}}(T,N_1)}{r_{\mathrm{f}}}(2z-x), x \in (z,\xi) \\ \sigma_{\mathrm{m}}(x) = 2\dfrac{V_{\mathrm{f}}}{V_{\mathrm{m}}}\dfrac{\tau_{\mathrm{i}}(T,N_1)}{r_{\mathrm{f}}}(2z-\xi) - 2\dfrac{V_{\mathrm{f}}}{V_{\mathrm{m}}}\dfrac{\tau_{\mathrm{i}}(T,N-N_1)}{r_{\mathrm{f}}}(x-\xi), x \in (\xi,y) \\ \sigma_{\mathrm{m}}(x) = 2\dfrac{V_{\mathrm{f}}}{V_{\mathrm{m}}}\dfrac{\tau_{\mathrm{i}}(T,N_1)}{r_{\mathrm{f}}}(2z-\xi) - 2\dfrac{V_{\mathrm{f}}}{V_{\mathrm{m}}}\dfrac{\tau_{\mathrm{i}}(T,N-N_1)}{r_{\mathrm{f}}}(2y-\xi-x), x \in (y,l_{\mathrm{d}}) \\ \sigma_{\mathrm{m}}(x) = \sigma_{\mathrm{mo}} - \left[\sigma_{\mathrm{mo}} - 2\dfrac{V_{\mathrm{f}}}{V_{\mathrm{m}}}\dfrac{\tau_{\mathrm{i}}(T,N_1)}{r_{\mathrm{f}}}(2z-\xi) + 2\dfrac{V_{\mathrm{f}}}{V_{\mathrm{m}}}\dfrac{\tau_{\mathrm{i}}(T,N-N_1)}{r_{\mathrm{f}}}(2y=\xi-l_{\mathrm{d}})\right]\exp\left(-\rho\dfrac{x-l_{\mathrm{d}}}{r_{\mathrm{f}}}\right), x \in \left(l_{\mathrm{d}}, \dfrac{l_{\mathrm{c}}}{2}\right) \end{cases} \tag{10}$$

$$\begin{cases} \tau_{\mathrm{i}}(x) = \tau_{\mathrm{i}}(T,N_1), x \in (0,z) \\ \tau_{\mathrm{i}}(x) = -\tau_{\mathrm{i}}(T,N_1), x \in (z,\xi) \\ \tau_i(x) = -\tau_{\mathrm{i}}(T,N-N_1), x \in (\xi,y) \\ \tau_{\mathrm{i}}(x) = \tau_{\mathrm{i}}(T,N-N_1), x \in (y,l_{\mathrm{d}}) \\ \tau_{\mathrm{i}}(x) = \dfrac{\rho}{2}\left[\dfrac{V_{\mathrm{m}}}{V_{\mathrm{f}}}\sigma_{\mathrm{mo}} - \dfrac{2\tau_{\mathrm{i}}(T,N_1)}{r_{\mathrm{f}}}(2z-\xi) + \dfrac{2\tau_{\mathrm{i}}(T,N-N_1)}{r_{\mathrm{f}}}(2y-\xi-l_{\mathrm{d}})\right]\exp\left(-\rho\dfrac{x-l_{\mathrm{d}}}{r_{\mathrm{f}}}\right), x \in \left(l_{\mathrm{d}}, \dfrac{l_{\mathrm{c}}}{2}\right) \end{cases} \tag{11}$$

where z denotes the fiber/matrix interface new-slip length.

(2) Interface debonding and slip lengths

The fiber/matrix interface debonded length and interface slip length are determined using the fracture mechanics approach, as shown by the following equation [35]

$$\zeta_{\mathrm{d}} = \frac{F}{4\pi r_{\mathrm{f}}}\frac{\partial w_{\mathrm{f}}(0)}{\partial l_{\mathrm{d}}} - \frac{1}{2}\int_0^{l_{\mathrm{d}}} \tau_{\mathrm{i}}(T)\frac{\partial v(x)}{\partial l_{\mathrm{d}}}dx \tag{12}$$

where ζ_{d} denotes the fiber/matrix interface debonded energy; $F(=\pi r_{\mathrm{f}}^2\sigma/V_{\mathrm{f}})$ is the fiber load at the matrix cracking plane; $w_{\mathrm{f}}(0)$ denotes the fiber axial displacement at the matrix crack plane; and $v(x)$ denotes the relative displacement between the fiber and the matrix.

$$\begin{aligned} w_{\mathrm{f}}(x) &= \int_x^{l_{\mathrm{c}}/2} \frac{\sigma_{\mathrm{f}}(x)}{E_{\mathrm{f}}}dx \\ &= \frac{\sigma}{V_{\mathrm{f}}E_{\mathrm{f}}}(l_{\mathrm{d}}-x) - \frac{\tau_{\mathrm{i}}(T,N_1)}{r_{\mathrm{f}}E_{\mathrm{f}}}\left(2\xi l_{\mathrm{d}} - \xi^2 - x^2\right) - \frac{\tau_{\mathrm{i}}(T,N-N_1)}{r_{\mathrm{f}}E_{\mathrm{f}}}(l_{\mathrm{d}}-\xi)^2 + \frac{\sigma_{\mathrm{fo}}}{E_{\mathrm{f}}}\left(\frac{l_{\mathrm{c}}}{2} - l_{\mathrm{d}}\right) \\ &\quad + \frac{r_{\mathrm{f}}}{\rho E_{\mathrm{f}}}\left[\frac{V_{\mathrm{m}}}{V_{\mathrm{f}}}\sigma_{\mathrm{mo}} - \frac{2\tau_{\mathrm{i}}(T,N_1)}{r_{\mathrm{f}}}\xi - \frac{2\tau_{\mathrm{i}}(T,N-N_1)}{r_{\mathrm{f}}}(l_{\mathrm{d}}-\xi)\right]\left[1-\exp\left(-\rho\frac{l_{\mathrm{c}}/2-l_{\mathrm{d}}}{r_{\mathrm{f}}}\right)\right] \end{aligned} \tag{13}$$

$$\begin{aligned} w_{\mathrm{m}}(x) &= \int_x^{l_c} \frac{\sigma_{\mathrm{m}}(x)}{E_{\mathrm{m}}}dx \\ &= \frac{V_{\mathrm{f}}\tau_i(T,N_1)}{r_{\mathrm{f}}V_{\mathrm{m}}E_m}\left(2\xi l_{\mathrm{d}} - \xi^2 - x^2\right) + \frac{V_{\mathrm{f}}\tau_i(T,N-N_1)}{r_{\mathrm{f}}V_{\mathrm{m}}E_m}(l_{\mathrm{d}}-\xi)^2 + \frac{\sigma_{\mathrm{mo}}}{E_{\mathrm{m}}}\left(\frac{l_{\mathrm{c}}}{2} - l_{\mathrm{d}}\right) \\ &\quad - \frac{r_{\mathrm{f}}}{\rho E_{\mathrm{m}}}\left[\sigma_{\mathrm{mo}} - 2\frac{V_{\mathrm{f}}\tau_i(T,N_1)}{r_{\mathrm{f}}V_{\mathrm{m}}}\xi - 2\frac{V_{\mathrm{f}}\tau_i(T,N-N_1)}{r_{\mathrm{f}}V_{\mathrm{m}}}(l_{\mathrm{d}}-\xi)\right]\left[1-\exp\left(-\rho\frac{l_{\mathrm{c}}/2-l_{\mathrm{d}}}{r_{\mathrm{f}}}\right)\right] \end{aligned} \tag{14}$$

The relative displacement $v(x)$ between the fiber and the matrix is determined with the following equation:

$$
\begin{aligned}
v(x) &= \left| w_{\mathrm{f}}(x) - w_{\mathrm{m}}(x) \right| \\
&= \frac{\sigma}{V_{\mathrm{f}} E_{\mathrm{f}}}(l_{\mathrm{d}} - x) - \frac{E_{\mathrm{c}} \tau_i(T, N_1)}{r_{\mathrm{f}} V_{\mathrm{m}} E_{\mathrm{m}} E_{\mathrm{f}}}\left(2\xi l_{\mathrm{d}} - \xi^2 - x^2\right) - \frac{E_{\mathrm{c}} \tau_i(T, N - N_1)}{r_{\mathrm{f}} V_{\mathrm{m}} E_{\mathrm{m}} E_{\mathrm{f}}}(l_{\mathrm{d}} - \xi)^2 \\
&+ \frac{r_{\mathrm{f}} E_{\mathrm{c}}}{\rho V_{\mathrm{m}} E_{\mathrm{m}} E_{\mathrm{f}}}\left[\sigma_{\mathrm{mo}} - 2\frac{\tau_i(T, N_1)}{r_{\mathrm{f}}}\xi - 2\frac{\tau_i(T, N - N_1)}{r_{\mathrm{f}}}(l_{\mathrm{d}} - \xi)\right]\left[1 - \exp\left(-\rho \frac{l_{\mathrm{c}}/2 - l_{\mathrm{d}}}{r_{\mathrm{f}}}\right)\right]
\end{aligned}
\tag{15}
$$

Substituting $w_{\mathrm{f}}(x = 0)$ and $v(x)$ into Eq. (12) leads to the form of the following equation:

$$
\begin{aligned}
&\frac{E_{\mathrm{c}}\left[\tau_{\mathrm{i}}(T, N - N_1)\right]^2}{r_{\mathrm{f}} V_{\mathrm{m}} E_{\mathrm{m}} E_{\mathrm{f}}}(l_{\mathrm{d}} - \xi)^2 + \frac{E_{\mathrm{c}}\left[\tau_{\mathrm{i}}(T, N - N_1)\right]^2}{\rho V_{\mathrm{m}} E_{\mathrm{m}} E_{\mathrm{f}}}(l_{\mathrm{d}} - \xi) - \frac{\tau_{\mathrm{i}}(T, N - N_1)\sigma}{V_{\mathrm{f}} E_{\mathrm{f}}}(l_{\mathrm{d}} - \xi) \\
&+ \frac{2E_{\mathrm{c}} \tau_{\mathrm{i}}(T, N_1)\tau_{\mathrm{i}}(T, N - N_1)}{r_{\mathrm{f}} V_{\mathrm{m}} E_{\mathrm{m}} E_{\mathrm{f}}}\xi(l_{\mathrm{d}} - \xi) - \frac{r_{\mathrm{f}} \tau_{\mathrm{i}}(T, N - N_1)\sigma}{2\rho V_{\mathrm{f}} E_{\mathrm{f}}} + \frac{E_{\mathrm{c}}\left[\tau_{\mathrm{i}}(T, N_1)\right]^2}{r_{\mathrm{f}} V_{\mathrm{m}} E_{\mathrm{m}} E_{\mathrm{f}}}\xi^2 \\
&+ \frac{E_{\mathrm{c}} \tau_{\mathrm{i}}(T, N_1)\tau_{\mathrm{i}}(T, N - N_1)}{\rho V_{\mathrm{m}} E_{\mathrm{m}} E_{\mathrm{f}}}\xi - \frac{\tau_{\mathrm{i}}(T, N_1)\sigma}{V_{\mathrm{f}} E_{\mathrm{f}}}\xi + \frac{r_{\mathrm{f}} V_{\mathrm{m}} E_{\mathrm{m}} \sigma^2}{4V_{\mathrm{f}}^2 E_{\mathrm{f}} E_{\mathrm{c}}} - \zeta_{\mathrm{d}} = 0
\end{aligned}
\tag{16}
$$

Solving Eq. (16), the fiber/matrix interface debonded length l_{d} is determined with the following equation:

$$
l_{\mathrm{d}} = \left(1 - \frac{\tau_i(T, N_1)}{\tau_i(T, N - N_1)}\right)\xi + \frac{r_{\mathrm{f}}}{2}\left(\frac{V_{\mathrm{m}} E_{\mathrm{m}} \sigma}{V_{\mathrm{f}} E_{\mathrm{c}} \tau_i(T, N - N_1)} - \frac{1}{\rho}\right) - \sqrt{\left(\frac{r_{\mathrm{f}}}{2\rho}\right)^2 + \frac{r_{\mathrm{f}} V_{\mathrm{m}} E_{\mathrm{m}} E_{\mathrm{f}}}{E_{\mathrm{c}}\left[\tau_i(T, N - N_1)\right]^2}\zeta_{\mathrm{d}}}
\tag{17}
$$

The fiber/matrix interface counter-slip length and new-slip length are determined with the following equations:

$$
y = \frac{1}{2}\left\{l_{\mathrm{d}}(\sigma_{\max}) + \left(1 - \frac{\tau_i(T, N_1)}{\tau_{\mathrm{i}}(T, N - N_1)}\right)\xi - \left[\frac{r_{\mathrm{f}}}{2}\left(\frac{V_{\mathrm{m}} E_{\mathrm{m}}}{V_{\mathrm{f}} E_{\mathrm{c}}}\frac{\sigma}{\tau_{\mathrm{i}}(T, N - N_1)} - \frac{1}{\rho}\right) - \sqrt{\left(\frac{r_{\mathrm{f}}}{2\rho}\right)^2 + \frac{r_{\mathrm{f}} V_{\mathrm{m}} E_{\mathrm{m}} E_{\mathrm{f}}}{E_{\mathrm{c}}\left[\tau_{\mathrm{i}}(T, N - N_1)\right]^2}\zeta_{\mathrm{d}}}\right]\right\}
\tag{18}
$$

$$
z = \frac{\tau_{\mathrm{i}}(T, N - N_1)}{\tau_i(T, N_1)}\left\{y(\sigma_{\min}) - \frac{1}{2}\left[\begin{aligned} &l_{\mathrm{d}} + \left(1 - \frac{\tau_i(T, N_1)}{\tau_{\mathrm{i}}(T, N - N_1)}\right)\xi \\ &- \left[\frac{r_{\mathrm{f}}}{2}\left(\frac{V_{\mathrm{m}} E_{\mathrm{m}}}{V_{\mathrm{f}} E_{\mathrm{c}}}\frac{\sigma}{\tau_{\mathrm{i}}(T, N - N_1)} - \frac{1}{\rho}\right) - \sqrt{\left(\frac{r_{\mathrm{f}}}{2\rho}\right)^2 + \frac{r_{\mathrm{f}} V_{\mathrm{m}} E_{\mathrm{m}} E_{\mathrm{f}}}{E_{\mathrm{c}}\left[\tau_{\mathrm{i}}(T, N - N_1)\right]^2}\zeta_{\mathrm{d}}}\right]\end{aligned}\right]\right\}
\tag{19}
$$

(3) Hysteresis-based damage models

When the damage forms within the composite, the composite strain is determined with Eq. (20), which assumes that the composite strain is equivalent to the average strain in an undamaged fiber.

$$
\varepsilon_{\mathrm{c}} = \frac{2}{E_{\mathrm{f}} l_{\mathrm{c}}}\int_{l_{\mathrm{c}}/2} \sigma_{\mathrm{f}}(x)\,dx - (\alpha_{\mathrm{lc}} - \alpha_{\mathrm{lf}})\Delta\mathrm{T}
\tag{20}
$$

where a_{lc} and a_{lf} denote the composite and fiber axial thermal expansion coefficient, respectively; and ΔT denotes the temperature difference between the fabricated temperature and testing temperature.

Under TMF loading at the peak stress of $\sigma_{\max1}$, the unloading and reloading composite strains can be determined using the following equations:

$$
\varepsilon_{\mathrm{unloading}} = \frac{\sigma}{V_{\mathrm{f}} E_{\mathrm{f}}} + 4\frac{\tau_{\mathrm{i}}(T, N_1)}{E_{\mathrm{f}}}\frac{y^2}{r_{\mathrm{f}} l_{\mathrm{c}}} - 2\frac{\tau_{\mathrm{i}}(T, N_1)}{E_{\mathrm{f}}}\frac{(2y - l_{\mathrm{d}})(2y + l_{\mathrm{d}} - l_{\mathrm{c}})}{r_{\mathrm{f}} l_{\mathrm{c}}} - (\alpha_{\mathrm{lc}} - \alpha_{\mathrm{lf}})\Delta\mathrm{T}
\tag{21}
$$

$$
\begin{aligned}
\varepsilon_{\mathrm{reloading}} &= \frac{\sigma}{V_{\mathrm{f}} E_{\mathrm{f}}} - 4\frac{\tau_{\mathrm{i}}(T, N_1)}{E_{\mathrm{f}}}\frac{z^2}{r_{\mathrm{f}} l_{\mathrm{c}}} + 4\frac{\tau_{\mathrm{i}}(T, N_1)}{E_{\mathrm{f}}}\frac{(y - 2z)^2}{r_{\mathrm{f}} l_{\mathrm{c}}} \\
&+ 2\frac{\tau_{\mathrm{i}}(T, N_1)}{E_{\mathrm{f}}}\frac{(l_{\mathrm{d}} - 2y + 2z)(l_{\mathrm{d}} + 2y - 2z - l_{\mathrm{c}})}{r_{\mathrm{f}} l_{\mathrm{c}}} - (\alpha_{\mathrm{lc}} - \alpha_{\mathrm{lf}})\Delta\mathrm{T}
\end{aligned}
\tag{22}
$$

Under TMF loading at the peak stress of $\sigma_{\max2}$, the unloading and reloading composite strains can be determined using the following equations:

$$\begin{aligned}\varepsilon_{\text{unloading}} = &\frac{2\sigma l_{\text{d}}}{V_{\text{f}} E_{\text{f}} l_{\text{c}}} + \frac{2\tau_i(T,N_1)}{r_{\text{f}} E_{\text{f}} l_{\text{c}}}\xi^2 + \frac{4\tau_i(T,N_1)}{r_{\text{f}} E_{\text{f}} l_{\text{c}}}\xi(l_{\text{d}}-\xi) + \frac{4\tau_i(T,N-N_1)}{r_{\text{f}} E_{\text{f}} l_{\text{c}}}(y-\xi)^2 \\ &- \frac{2\tau_i(T,N-N_1)}{r_{\text{f}} E_{\text{f}} l_{\text{c}}}(2y-\xi-l_{\text{d}})^2 + \frac{2\sigma_{\text{fo}}}{E_{\text{f}} l_{\text{c}}}\left(\frac{l_{\text{c}}}{2}-l_{\text{d}}\right) \\ &+ \frac{2r_{\text{f}}}{\rho E_{\text{f}} l_{\text{c}}}\left[\frac{V_{\text{m}}}{V_{\text{f}}}\sigma_{\text{mo}} + \frac{2\tau_i(T,N_1)}{r_{\text{f}}}\xi + \frac{2\tau_i(T,N-N_1)}{r_{\text{f}}}(2y-\xi-l_{\text{d}})\right] \\ &\times\left[1-\exp\left(-\rho\frac{l_{\text{c}}/2-l_{\text{d}}}{r_{\text{f}}}\right)\right] - (\alpha_{\text{lc}}-\alpha_{\text{lf}})\Delta \text{T}\end{aligned} \tag{23}$$

$$\begin{aligned}\varepsilon_{\text{reloading}} = &\frac{2\sigma}{V_{\text{f}} E_{\text{f}} l_{\text{c}}} l_{\text{d}} - \frac{4\tau_i(T,N_1)}{r_{\text{f}} E_{\text{f}} l_{\text{c}}}z^2 + \frac{2\tau_i(T,N_1)}{r_{\text{f}} E_{\text{f}} l_{\text{c}}}(2z-\xi)^2 - \frac{4\tau_i(T,N_1)}{r_{\text{f}} E_{\text{f}} l_{\text{c}}}(2z-\xi)(l_{\text{d}}-\xi) \\ &+ \frac{4\tau_i(T,N-N_1)}{r_{\text{f}} E_{\text{f}} l_{\text{c}}}(y-\xi)^2 - \frac{2\tau_i(T,N-N_1)}{r_{\text{f}} E_{\text{f}} l_{\text{c}}}(2y-\xi-l_{\text{d}})^2 + \frac{2\sigma_{\text{fo}}}{E_{\text{f}} l_{\text{c}}}\left(\frac{l_{\text{c}}}{2}-l_{\text{d}}\right) \\ &+ \frac{2r_{\text{f}}}{\rho E_{\text{f}} l_{\text{c}}}\left[\frac{V_{\text{m}}}{V_{\text{f}}}\sigma_{\text{mo}} - \frac{2\tau_i(T,N_1)}{r_{\text{f}}}(2z-\xi) + \frac{2\tau_i(T,N-N_1)}{r_{\text{f}}}(2y-\xi-l_{\text{d}})\right] \\ &\times\left[1-\exp\left(-\rho\frac{l_{\text{c}}/2-l_{\text{d}}}{r_{\text{f}}}\right)\right] - (\alpha_{\text{lc}}-\alpha_{\text{lf}})\Delta \text{T}\end{aligned} \tag{24}$$

Under TMF loading, the area associated with the hysteresis loops is the dissipated energy during the corresponding cycle, which can be described using the following equation:

$$U_{\text{e}}(\sigma_{\max},T,N) = \int_{\sigma_{\min}}^{\sigma_{\max}}\left[\varepsilon_{\text{unloading}}(\sigma_{\max},T,N) - \varepsilon_{\text{reloading}}(\sigma_{\max},T,N)\right]d\sigma \tag{25}$$

With substitution of the unloading and reloading strains of Eq. (21), (22), (23) and (24) into Eq. (25), the TMF hysteresis dissipated energy corresponding to different loading sequences can be obtained.

The hysteresis modulus E is described using the following equation:

$$E = \frac{\sigma_{\max}-\sigma_{\min}}{\varepsilon_{\text{c}}(\sigma_{\max})-\varepsilon_{\text{c}}(\sigma_{\min})} \tag{26}$$

The damage evolution of SiC/SiC composite under TMF loading with the phase angles of $\theta = 0$, $\pi/3$, $\pi/2$ and π, and five different loading modes (i.e. Case I: $\sigma_{max} = 200$ MPa; Case II: $\sigma_{max1} = 150$ MPa and $\sigma_{max2} = 200$ MPa; Case III: $\sigma_{max1} = 180$ MPa and $\sigma_{max2} = 200$ MPa; Case IV: $\sigma_{max1} = 220$ MPa and $\sigma_{max2} = 200$ MPa; Case V: $\sigma_{max1} = 250$ MPa and $\sigma_{max2} = 200$ MPa) are shown in Fig. 2 ~ 5. The ceramic composite system of SiC/SiC is used for the case study and its material properties are given by: $V_f = 30$ %, $E_f = 230$ GPa, $E_m = 300$ GPa, $r_f = 7.5$ μm, $\zeta_d = 1$ J/m^2, $a_{rf} = 2.9 \times 10^{-6}$/K, $a_{lf} = 3.9 \times 10^{-6}$/K, $a_{rm} = 4.6 \times 10^{-6}$/K, $a_{lm} = 2.0 \times 10^{-6}$/K, $T_1 = 100$ °C and $T_2 = 1000$ °C.

(a) $\theta = 0$

When the phase angle is $\theta = 0$, the evolution of TMF hysteresis dissipated energy (U_e), hysteresis modulus (E), peak strain (ε_{max}), fiber/matrix interface debonding length ($2l_d/l_c$), fiber/matrix interface sliding length ($2y/l_c$) and fiber/matrix interface debonding ratio ($l_d(\sigma_{max1})/l_d(\sigma_{max2})$) with increasing applied cycles for different loading sequences are shown in Fig. 2 and listed in Table 1.

The TMF hysteresis dissipated energy (U_e) increases with applied cycles for five different loading sequences. For the loading sequence of Case I ($\sigma_{max} = 200$ MPa), the hysteresis dissipated energy increases from $U_e = 9.4$ kJ/m^3 at the first applied cycle to $U_e = 26.1$ kJ/m^3 at the 10 000th applied cycle; for the loading sequence of Case II ($\sigma_{max1} = 150$ MPa and $\sigma_{max2} = 200$ MPa), the TMF hysteresis dissipated energy increases from $U_e = 9.7$ kJ/m^3 at the first applied cycle to $U_e = 26.1$ kJ/m^3 at the 10 000th applied cycle; for the loading sequence of Case III ($\sigma_{max1} = 180$ MPa and $\sigma_{max2} = 200$ MPa), the TMF hysteresis dissipated energy increases from $U_e = 10.9$ kJ/m^3 at the first applied cycle to $U_e = 26.1$ kJ/m^3 at the 10 000th applied cycle; for the loading sequence of Case IV ($\sigma_{max1} = 220$ MPa and $\sigma_{max2} = 200$ MPa), the TMF hysteresis dissipated energy increases from $U_e = 14.2$ kJ/m^3 at the first applied cycle to $U_e = 26.1$ kJ/m^3 at the 10 000th applied cycle; and for the loading sequence of Case V ($\sigma_{max1} = 250$ MPa and $\sigma_{max2} = 200$ MPa), the TMF hysteresis dissipated energy increases from $U_e = 16.7$ kJ/m^3 at the first applied cycle to $U_e = 26.1$ kJ/m^3 at the 10 000th applied cycle, as shown in Fig. 2(a).

The TMF hysteresis modulus (E) decreases with applied cycles for five different loading sequences. For the loading sequence of Case I ($\sigma_{max} = 200$ MPa), the TMF hysteresis modulus decreases from $E = 193.8$ GPa at the first applied cycle to $E = 118.8$ GPa at the 10 000th applied cycle; for the loading sequence of Case II ($\sigma_{max1} = 150$ MPa and $\sigma_{max2} = 200$ MPa), the TMF hysteresis modulus decreases from $E = 180.5$ GPa at the first applied cycle to $E = 118.8$ GPa at the 10 000th applied cycle; for the loading sequence

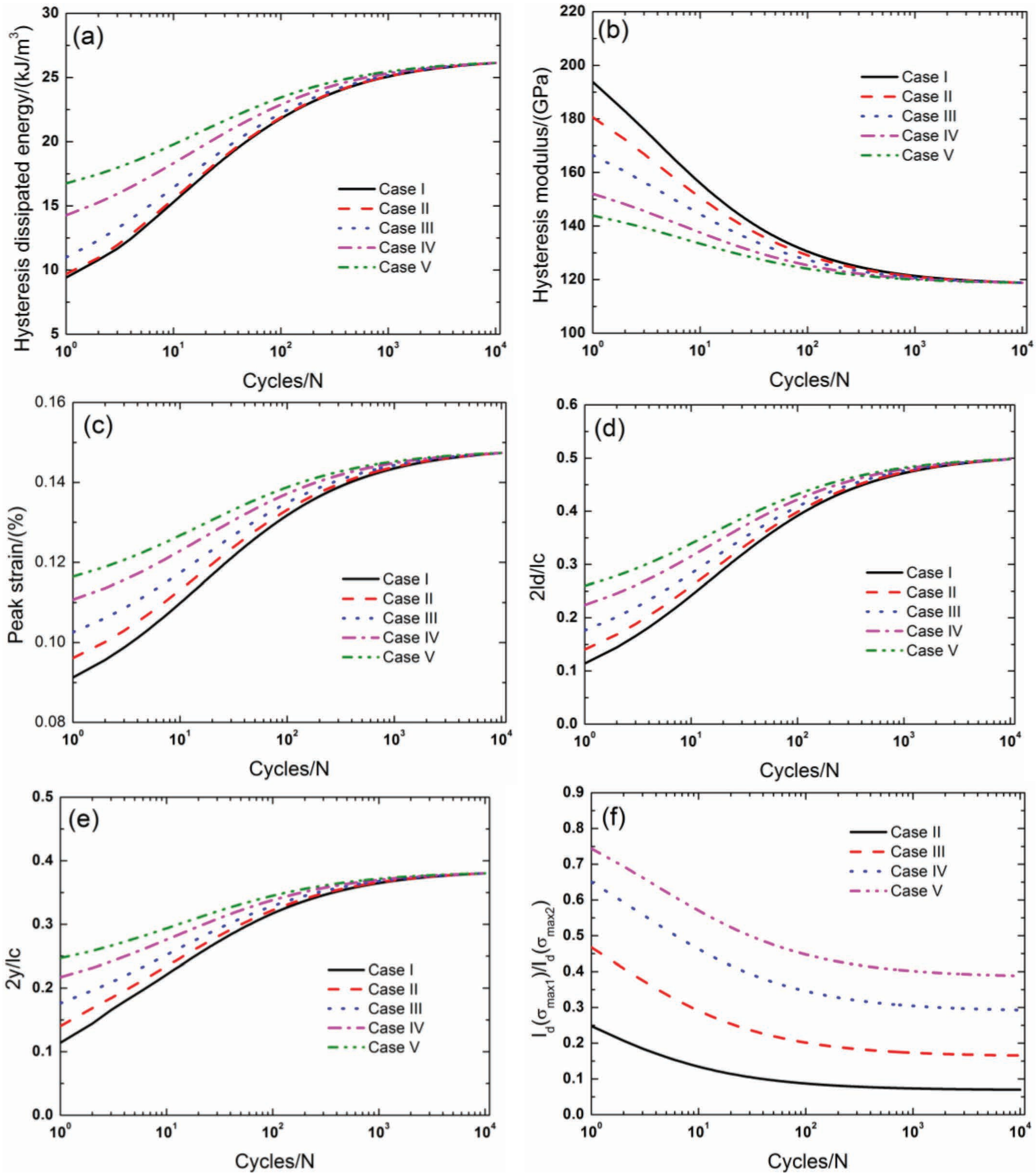

Fig. 2: The damage evolution of SiC/SiC composite under in-phase thermomechanical fatigue loading with five different loading modes (Case I: σ_{max} = 200 MPa; Case II: σ_{max1} = 150 MPa and σ_{max2} = 200 MPa; Case III: σ_{max1} = 180 MPa and σ_{max2} = 200 MPa; Case IV: σ_{max1} = 220 MPa and σ_{max2} = 200 MPa; Case V: σ_{max1} = 250 MPa and σ_{max2} = 200 MPa) corresponding to (a) the TMF hysteresis dissipated energy versus cycle number curves; (b) the TMF hysteresis modulus versus cycle number curves; (c) the TMF peak strain versus cycle number curves; (d) the fiber/matrix interface debonding length ($2l_d/l_c$) versus cycle number curves; (e) the fiber/matrix interface sliding length ($2y/l_c$) versus cycle number curves; and (f) the fiber/matrix interface debonding ratio ($l_d(\sigma_{max1})/l_d(\sigma_{max2})$) for different peak stress versus cycle number curves.

Table 1: The TMF damage evolution of SiC/SiC composite at the phase angle of θ = 0 for different loading sequences.

θ = 0	Case I		Case II		Case III		Case IV		Case V	
	$N = 1$	$N = 10\,000$	$N = 1$	$N = 10\,000$	$N = 1$	$N = 10\,000$	$N = 1$	$N = 10\,000$	$N = 1$	$N = 10\,000$
$U_e/(\mathrm{kJ/m^3})$	9.4	26.1	9.7	26.1	10.9	26.1	14.2	26.1	16.7	26.1
$E/(\mathrm{GPa})$	193.8	118.8	180.5	118.8	166.3	118.8	152	118.8	143.9	118.8
$\varepsilon_{max}/(\%)$	0.091	0.14	0.096	0.14	0.102	0.14	0.11	0.14	0.116	0.14
$2l_d/l_c$	0.114	0.498	0.14	0.498	0.176	0.498	0.224	0.498	0.26	0.498
$2y/l_c$	0.114	0.38	0.14	0.38	0.176	0.38	0.217	0.38	0.246	0.38
$l_d(\sigma_{max1})/l_d(\sigma_{max2})$	–	–	0.24	0.07	0.46	0.16	0.65	0.29	0.74	0.38

of Case III (σ_{max1} = 180 MPa and σ_{max2} = 200 MPa), the TMF hysteresis modulus decreases from E = 166.3 GPa at the first applied cycle to E = 118.8 GPa at the 10 000th applied cycle; for the loading sequence of Case IV (σ_{max1} = 220 MPa and σ_{max2} = 200 MPa), the TMF hysteresis modulus decreases from E = 152 GPa at the first applied cycle to E = 118.8 GPa at the 10 000th applied cycle; and for the loading sequence of Case V (σ_{max1} = 250 MPa and σ_{max2} = 200 MPa), the TMF hysteresis modulus decreases from E = 143.9 GPa at the first applied cycle to E = 118.8 GPa at the 10 000th applied cycle, as shown in Fig. 2(b).

The TMF peak strain (ε_{max}) increases with applied cycles for five different loading sequences. For the loading sequence of Case I (σ_{max} = 200 MPa), the TMF peak strain increases from ε_{max} = 0.091 % at the first applied cycle to ε_{max} = 0.14 % at the 10 000th applied cycle; for the loading sequence of Case II (σ_{max1} = 150 MPa and σ_{max2} = 200 MPa), the TMF peak strain increases from ε_{max} = 0.096 % at the first applied cycle to ε_{max} = 0.14 % at the 10 000th applied cycle; for the loading sequence of Case III (σ_{max1} = 180 MPa and σ_{max2} = 200 MPa), the TMF peak strain increases from ε_{max} = 0.102 % at the first applied cycle to ε_{max} = 0.14 % at the 10 000th applied cycle; for the loading sequence of Case IV (σ_{max1} = 220 MPa and σ_{max2} = 200 MPa), the TMF peak strain increases from ε_{max} = 0.11 % at the first applied cycle to ε_{max} = 0.14 % at the 10 000th applied cycle; and for the loading sequence of Case V (σ_{max1} = 250 MPa and σ_{max2} =200 MPa), the TMF peak strain increases from ε_{max} = 0.116 % at the first applied cycle to ε_{max} = 0.14 % at the 10 000th applied cycle, as shown in Fig. 2(c).

The fiber/matrix interface debonding length ($2l_d/l_c$) increases with applied cycles for five different loading sequences. For the loading sequence of Case I (σ_{max} = 200 MPa), the fiber/matrix interface debonded length increases from $2l_d/l_c$ = 0.114 at the first applied cycle to $2l_d/l_c$ = 0.498 at the 10 000th applied cycle; for the loading sequence of Case II (σ_{max1} = 150 MPa and σ_{max2} = 200 MPa), the fiber/matrix interface debonded length increases from $2l_d/l_c$ = 0.14 at the first applied cycle to $2l_d/l_c$ = 0.498 at the 10 000th applied cycle; for the loading sequence of Case III (σ_{max1} = 180 MPa and σ_{max2} = 200 MPa), the fiber/matrix interface debonded length increases from $2l_d/l_c$ = 0.176 at the first applied cycle to $2l_d/l_c$ = 0.498 at the 10 000th applied cycle; for the loading sequence of Case IV (σ_{max1} = 220 MPa and σ_{max2} = 200 MPa), the fiber/matrix interface debonded length increases from $2l_d/l_c$ = 0.224 at the first applied cycle to $2l_d/l_c$ = 0.498 at the 10 000th applied cycle; and for the loading sequence of Case V (σ_{max1} = 250 MPa and σ_{max2} = 200 MPa), the fiber/matrix interface debonded length increases from $2l_d/l_c$ = 0.26 at the first applied cycle to $2l_d/l_c$ = 0.498 at the 10 000th applied cycle, as shown in Fig. 2(d).

The fiber/matrix interface sliding length ($2y/l_c$) increases with applied cycles for five different loading sequences. For the loading sequence of Case I (σ_{max} = 200 MPa), the fiber/matrix interface sliding length increases from $2y/l_c$ = 0.114 at the first applied cycle to $2y/l_c$ = 0.38 at the 10 000th applied cycle; for the loading sequence of Case II (σ_{max1} = 150 MPa and σ_{max2} = 200 MPa), the fiber/matrix interface sliding length increases from $2y/l_c$ = 0.14 at the first applied cycle to $2y/l_c$ = 0.38 at the 10 000th applied cycle; for the loading sequence of Case III (σ_{max1} = 180 MPa and σ_{max2} = 200 MPa), the fiber/matrix interface sliding length increases from $2y/l_c$ = 0.176 at the first applied cycle to $2y/l_c$ = 0.38 at the 10 000th applied cycle; for the loading sequence of Case IV (σ_{max1} =220 MPa and σ_{max2} = 200 MPa), the fiber/matrix interface sliding length increases from $2y/l_c$ = 0.217 at the first applied cycle to $2y/l_c$ = 0.38 at the 10 000th applied cycle; and for the loading sequence of Case V (σ_{max1} = 250 MPa and σ_{max2} = 200 MPa), the fiber/matrix interface sliding length increases from $2y/l_c$ = 0.246 at the first applied cycle to $2y/l_c$ = 0.38 at the 10 000th applied cycle, as shown in Fig. 2(e).

The fiber/matrix interface debonding ratio ($l_d(\sigma_{max1})/l_d(\sigma_{max2})$) for different peak stress decreases with increasing applied cycle for multiple loading sequence. For the loading sequence of Case II (σ_{max1} = 150 MPa and σ_{max2} = 200 MPa), the fiber/matrix interface debonding ratio decreases from $l_d(\sigma_{max1})/l_d(\sigma_{max2})$ = 0.24 at the first applied cycle to $l_d(\sigma_{max1})/l_d(\sigma_{max2})$ = 0.07 at the 10 000th applied cycle; for the loading sequence of Case III (σ_{max1} = 180 MPa and σ_{max2} = 200 MPa), the fiber/matrix interface debonding ratio decreases from $l_d(\sigma_{max1})/l_d(\sigma_{max2})$ = 0.46 at the first applied cycle to $l_d(\sigma_{max1})/l_d(\sigma_{max2})$ = 0.16 at the 10 000th applied cycle; for the loading sequence of Case IV (σ_{max1} = 220 MPa and σ_{max2} = 200 MPa), the fiber/matrix interface debonding ratio decreases from $l_d(\sigma_{max1})/l_d(\sigma_{max2})$ = 0.65 at the first applied cycle to $l_d(\sigma_{max1})/l_d(\sigma_{max2})$ = 0.29 at the 10 000th applied cycle; and for the loading sequence of Case V (σ_{max1} = 250 MPa and

σ_{max2} = 200 MPa), the fiber/matrix interface debonding ratio decreases from $l_d(\sigma_{max1})/l_d(\sigma_{max2})$ = 0.74 at the first applied cycle to $l_d(\sigma_{max1})/l_d(\sigma_{max2})$ = 0.38 at the 10 000th applied cycle, as shown in Fig. 2(f).

(b) $\theta = \pi/3$

When the phase angle is $\theta = \pi/3$, the evolution of TMF hysteresis dissipated energy (U_e), hysteresis modulus (E), peak strain (ε_{max}), fiber/matrix interface debonding length ($2l_d/l_c$), fiber/matrix interface sliding length ($2y/l_c$) and fiber/matrix interface debonding ratio ($l_d(\sigma_{max1})/l_d(\sigma_{max2})$) with increasing applied cycles for different loading sequences are shown in Fig. 3 and listed in Table 2.

The TMF hysteresis dissipated energy (U_e) increases with applied cycles for five different loading sequences. For the loading sequence of Case I (σ_{max} = 200 MPa), the TMF hysteresis dissipated energy increases from U_e = 15 kJ/m^3 at the first applied cycle to U_e = 34.5 kJ/m^3 at the 10 000th applied cycle; for the loading sequence of Case II (σ_{max1} = 150 MPa and σ_{max2} = 200 MPa), the TMF hysteresis dissipated energy increases from U_e = 16.2 kJ/m^3 at the first applied cycle to U_e = 34.5 kJ/m^3 at the 10 000th applied cycle; for the loading sequence of Case III (σ_{max1} = 180 MPa and σ_{max2} = 200 MPa), the TMF hysteresis dissipated energy increases from U_e = 18.6 kJ/m^3 at the first applied cycle to U_e = 34.5 kJ/m^3 at the 10 000th applied cycle; for the loading sequence of Case IV (σ_{max1} = 220 MPa and σ_{max2} = 200 MPa), the TMF hysteresis dissipated energy increases from U_e = 22.6 kJ/m^3 at the first applied cycle to U_e = 34.5 kJ/m^3 at the 10 000th applied cycle; and for the loading sequence of Case V (σ_{max1} = 250 MPa and σ_{max2} = 200 MPa), the TMF hysteresis dissipated energy increases from U_e = 25.9 kJ/m^3 at the first applied cycle to U_e = 34.5 kJ/m^3 at the 10 000th applied cycle, as shown in Fig. 3(a).

The TMF hysteresis modulus (E) decreases with applied cycles for five different loading sequences. For the loading sequence of Case I (σ_{max} = 200 MPa), the TMF hysteresis modulus decreases from E = 220.3 GPa at the first applied cycle to E = 167.4 GPa at the 10 000th applied cycle; for the loading sequence of Case II (σ_{max1} = 150 MPa and σ_{max2} = 200 MPa), the TMF hysteresis modulus decreases from E = 210.3 GPa at the first applied cycle to E = 167.4 GPa at the 10 000th applied cycle; for the loading sequence of Case III (σ_{max1} = 180 MPa and σ_{max2} = 200 MPa), the TMF hysteresis modulus decreases from E = 198.6 GPa at the first applied cycle to E = 167.4 GPa at the 10 000th applied cycle; for the loading sequence of Case IV (σ_{max1} = 220 MPa and σ_{max2} = 200 MPa), the TMF hysteresis modulus decreases from E = 186.6 GPa at the first applied cycle to E = 167.4 GPa at the 10 000th applied cycle; and for the loading sequence of Case V (σ_{max1} = 250 MPa and σ_{max2} = 200 MPa), the TMF hysteresis modulus decreases from E = 179.9 GPa at the first applied cycle to E = 167.4 GPa at the 10 000th applied cycle, as shown in Fig. 3(b).

The TMF peak strain (ε_{max}) increases with applied cycles for five different loading sequences. For the loading sequence of Case I (σ_{max} = 200 MPa), the TMF peak strain increases from ε_{max} = 0.083 % at the first applied cycle to ε_{max} = 0.103 % at the 10 000th applied cycle; for the loading sequence of Case II (σ_{max1} = 150 MPa and σ_{max2} =200 MPa), the TMF peak strain increases from ε_{max} = 0.086 % at the first applied cycle to ε_{max} = 0.103 % at the 10 000th applied cycle; for the loading sequence of Case III (σ_{max1} = 180 MPa and σ_{max2} = 200 MPa), the TMF peak strain increases from ε_{max} = 0.089 % at the first applied cycle to ε_{max} = 0.103 % at the 10 000th applied cycle; for the loading sequence of Case IV (σ_{max1} = 220 MPa and σ_{max2} = 200 MPa), the TMF peak strain increases from ε_{max} = 0.093 % at the first applied cycle to ε_{max} = 0.103 % at the 10 000th applied cycle; and for the loading sequence of Case V (σ_{max1} = 250 MPa and σ_{max2} = 200 MPa), the TMF peak strain increases from ε_{max} =0.096 % at the first applied cycle to ε_{max} = 0.103 % at the 10 000th applied cycle, as shown in Fig. 3(c).

The fiber/matrix interface debonding length ($2l_d/l_c$) increases with applied cycles for five different loading sequences. For the loading sequence of Case I (σ_{max} = 200 MPa), the fiber/matrix interface debonded length increases from $2l_d/l_c$ = 0.095 at the first applied cycle to $2l_d/l_c$ = 0.288 at the 10 000th applied cycle; for the loading sequence of Case II (σ_{max1} = 150 MPa and σ_{max2} = 200 MPa), the fiber/matrix interface debonded length increases from $2l_d/l_c$ = 0.113 at the first applied cycle to $2l_d/l_c$ = 0.288 at the 10 000th applied cycle; for the loading sequence of Case III (σ_{max1} = 180 MPa and σ_{max2} = 200 MPa), the fiber/matrix interface debonded length increases from $2l_d/l_c$ = 0.139 at the first applied cycle to $2l_d/l_c$ = 0.288 at the 10 000th applied cycle; for the loading sequence of Case IV (σ_{max1} = 220 MPa and σ_{max2} = 200 MPa), the fiber/matrix interface debonded length increases from $2l_d/l_c$ = 0.174 at the first applied cycle to $2l_d/l_c$ = 0.288 at the 10 000th applied cycle; and for the loading sequence of Case V (σ_{max1} = 250 MPa and σ_{max2} = 200 MPa), the fiber/matrix interface debonded length increases from $2l_d/l_c$ = 0.2 at the first applied cycle to $2l_d/l_c$ = 0.288 at the 10 000th applied cycle, as shown in Fig. 3(d).

The fiber/matrix interface sliding length ($2y/l_c$) increases with applied cycles for five different loading sequences. For the loading sequence of Case I (σ_{max} = 200 MPa), the fiber/matrix interface sliding length increases from $2y/l_c$ = 0.095 at the first applied cycle to $2y/l_c$ = 0.288 at the 10 000th applied cycle; for the loading sequence of Case II (σ_{max1} = 150 MPa and σ_{max2} = 200 MPa), the fiber/matrix interface sliding length increases from $2y/l_c$ = 0.113 at the first applied cycle to $2y/l_c$ = 0.288 at the 10 000th applied cycle; for the loading sequence of Case III (σ_{max1} = 180 MPa and σ_{max2} = 200 MPa), the fiber/matrix interface sliding length increases from $2y/l_c$ = 0.139 at the first applied cycle to $2y/l_c$ = 0.288 at the 10 000th applied cycle; for the loading sequence of Case IV (σ_{max1} = 220 MPa and σ_{max2} = 200 MPa), the fiber/matrix interface sliding length increases from $2y/l_c$ = 0.174 at the first applied cycle to $2y/l_c$ = 0.288 at the 10 000th applied cycle; and for the loading sequence of Case V (σ_{max1} = 250 MPa and σ_{max2} = 200 MPa), the fiber/matrix interface sliding length increases from $2y/l_c$ = 0.2 at the first applied cycle to $2y/l_c$ = 0.288 at the 10 000th applied cycle, as shown in Fig. 3(e).

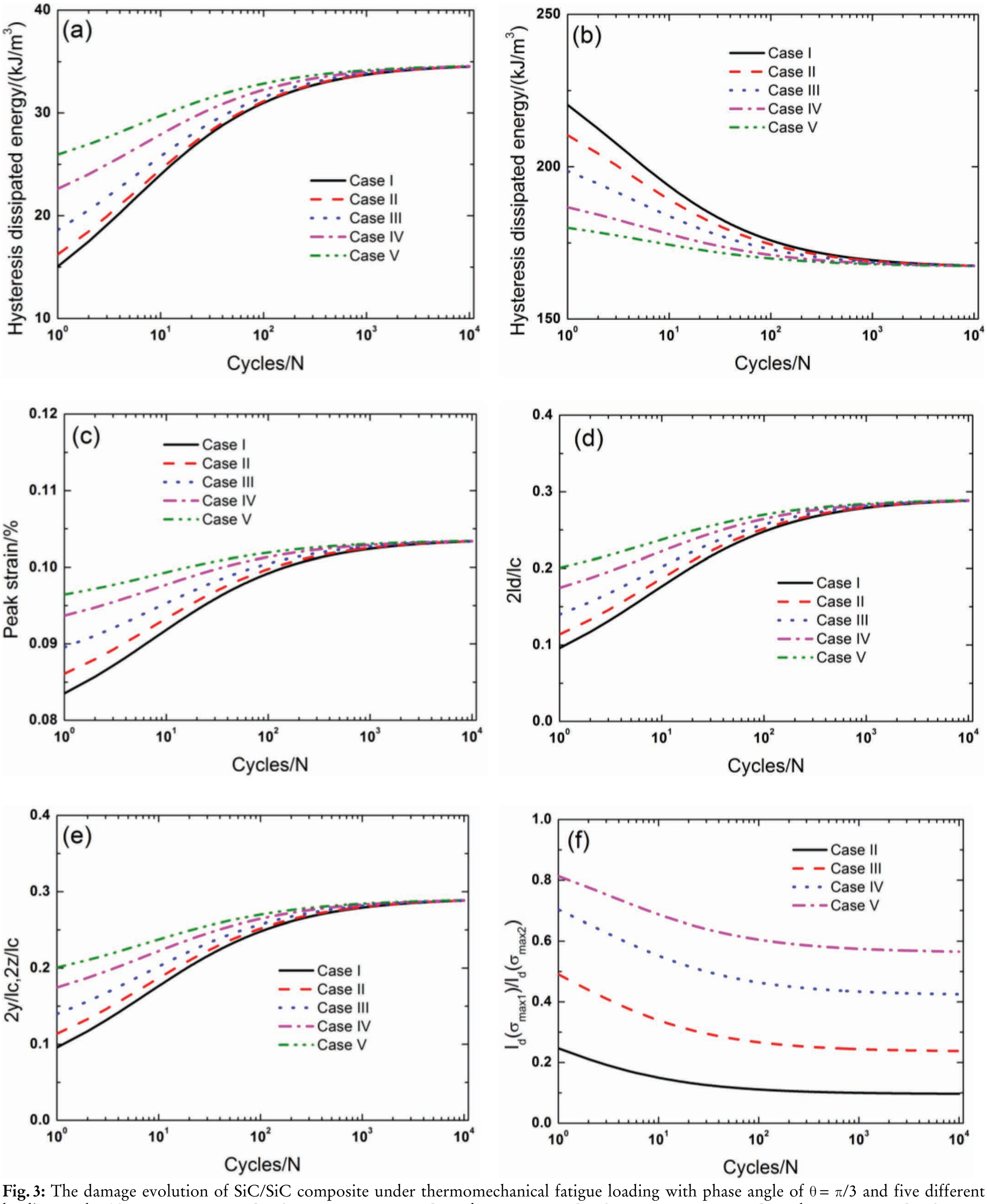

Fig. 3: The damage evolution of SiC/SiC composite under thermomechanical fatigue loading with phase angle of $\theta = \pi/3$ and five different loading modes (Case I: $\sigma_{max} = 200$ MPa; Case II: $\sigma_{max1} = 150$ MPa and $\sigma_{max2} = 200$ MPa; Case III: $\sigma_{max1} = 180$ MPa and $\sigma_{max2} = 200$ MPa; Case IV: $\sigma_{max1} = 220$ MPa and $\sigma_{max2} = 200$ MPa; Case V: $\sigma_{max1} = 250$ MPa and $\sigma_{max2} = 200$ MPa) corresponding to (a) the TMF hysteresis dissipated energy versus cycle number curves; (b) the TMF hysteresis modulus versus cycle number curves; (c) the TMF peak strain versus cycle number curves; (d) the fiber/matrix interface debonding length ($2l_d/l_c$) versus cycle number curves; (e) the fiber/matrix interface sliding length ($2y/l_c$) versus cycle number curves; and (f) the fiber/matrix interface debonding ratio ($l_d(\sigma_{max1})/l_d(\sigma_{max2})$) for different peak stress versus cycle number curves.

Table 2: The TMF damage evolution of SiC/SiC composite at the phase angle of θ = π/3 for different loading sequences.

θ = π/3	Case I		Case II		Case III		Case IV		Case V	
	N = 1	N = 10 000	N = 1	N = 10 000	N = 1	N = 10 000	N = 1	N = 10 000	N = 1	N = 10 000
$U_e/(\mathrm{kJ/m^3})$	15	34.5	16.2	34.5	18.6	34.5	22.6	34.5	25.9	34.5
$E/(\mathrm{GPa})$	220.3	167.4	210.3	167.4	198.6	167.4	186.6	167.4	179.9	167.4
$\varepsilon_{max}/(\%)$	0.083	0.103	0.086	0.103	0.089	0.103	0.093	0.103	0.096	0.103
$2l_d/l_c$	0.095	0.288	0.113	0.288	0.139	0.288	0.174	0.288	0.2	0.288
$2y/l_c$	0.095	0.288	0.113	0.288	0.139	0.288	0.174	0.288	0.2	0.288
$l_d(\sigma_{max1})/l_d(\sigma_{max2})$	–	–	0.246	0.097	0.49	0.23	0.7	0.42	0.81	0.56

The fiber/matrix interface debonding ratio ($l_d(\sigma_{max1})/l_d(\sigma_{max2})$) for different peak stress decreases with increasing applied cycle for multiple loading sequence. For the loading sequence of Case II (σ_{max1} = 150 MPa and σ_{max2} = 200 MPa), the fiber/matrix interface debonding ratio decreases from $l_d(\sigma_{max1})/l_d(\sigma_{max2})$ = 0.246 at the first applied cycle to $l_d(\sigma_{max1})/l_d(\sigma_{max2})$ = 0.097 at the 10 000th applied cycle; for the loading sequence of Case III (σ_{max1} = 180 MPa and σ_{max2} = 200 MPa), the fiber/matrix interface debonding ratio decreases from $l_d(\sigma_{max1})/l_d(\sigma_{max2})$ = 0.49 at the first applied cycle to $l_d(\sigma_{max1})/l_d(\sigma_{max2})$ = 0.23 at the 10 000th applied cycle; for the loading sequence of Case IV (σ_{max1} = 220 MPa and σ_{max2} = 200 MPa), the fiber/matrix interface debonding ratio decreases from $l_d(\sigma_{max1})/l_d(\sigma_{max2})$ = 0.7 at the first applied cycle to $l_d(\sigma_{max1})/l_d(\sigma_{max2})$ = 0.42 at the 10 000th applied cycle; and for the loading sequence of Case V (σ_{max1} = 250 MPa and σ_{max2} = 200 MPa), the fiber/matrix interface debonding ratio decreases from $l_d(\sigma_{max1})/l_d(\sigma_{max2})$ = 0.81 at the first applied cycle to $l_d(\sigma_{max1})/l_d(\sigma_{max2})$ = 0.56 at the 10 000th applied cycle, as shown in Fig. 3(f).

(c) θ=π/2

When the phase angle is $\theta = \pi/2$, the evolution of TMF hysteresis dissipated energy (U_e), hysteresis modulus (E), peak strain (ε_{max}), fiber/matrix interface debonding length ($2l_d/l_c$), fiber/matrix interface sliding length ($2y/l_c$) and fiber/matrix interface debonding ratio ($l_d(\sigma_{max1})/l_d(\sigma_{max2})$) with increasing applied cycles for different loading sequences are shown in Fig. 4 and listed in Table 3.

The TMF hysteresis dissipated energy (U_e) increases with applied cycles for five different loading sequences. For the loading sequence of Case I (σ_{max} =200 MPa), the TMF hysteresis dissipated energy increases from U_e = 24.7 kJ/m^3 at the first applied cycle to U_e = 59 kJ/m^3 at the 10 000th applied cycle; for the loading sequence of Case II (σ_{max1} = 150 MPa and σ_{max2} = 200 MPa), the TMF hysteresis dissipated energy increases from U_e = 27.2 kJ/m^3 at the first applied cycle to U_e = 59 kJ/m^3 at the 10 000th applied cycle; for the loading sequence of Case III (σ_{max1} = 180 MPa and σ_{max2} = 200 MPa), the TMF hysteresis dissipated energy increases from U_e = 31.6 kJ/m^3 at the first applied cycle to U_e = 59 kJ/m^3 at the 10 000th applied cycle; for the loading sequence of Case IV (σ_{max1} = 220 MPa and σ_{max2} = 200 MPa), the TMF hysteresis dissipated energy increases from U_e = 38.3 kJ/m^3 at the first applied cycle to U_e = 59 kJ/m^3 at the 10 000th applied cycle; and for the loading sequence of Case V (σ_{max1} = 250 MPa and σ_{max2} = 200 MPa), the TMF hysteresis dissipated energy increases from U_e = 43.8 kJ/m^3 at the first applied cycle to U_e = 59 kJ/m^3 at the 10 000th applied cycle, as shown in Fig. 4(a).

The TMF hysteresis modulus (E) decreases with applied cycles for five different loading sequences. For the loading sequence of Case I (σ_{max} = 200 MPa), the TMF hysteresis modulus decreases from E = 233.6 GPa at the first applied cycle to E = 190.3 GPa at the 10 000th applied cycle; for the loading sequence of Case II (σ_{max1} = 150 MPa and σ_{max2} = 200 MPa), the TMF hysteresis modulus decreases from E = 225.2 GPa at the first applied cycle to E = 190.3 GPa at the 10 000th applied cycle; for the loading sequence of Case III (σ_{max1} = 180 MPa and σ_{max2} = 200 MPa), the TMF hysteresis modulus decreases from E = 215 GPa at the first applied cycle to E = 190.3 GPa at the 10 000th applied cycle; for the loading sequence of Case IV (σ_{max1} = 220 MPa and σ_{max2} = 200 MPa), the TMF hysteresis modulus decreases from E = 204.5 GPa at the first applied cycle to E = 190.3 GPa at the 10 000th applied cycle; and for the loading sequence of Case V (σ_{max1} = 250 MPa and σ_{max2} = 200 MPa), the TMF hysteresis modulus decreases from E = 198.7 GPa at the first applied cycle to E = 190.3 GPa at the 10 000th applied cycle, as shown in Fig. 4(b).

The TMF peak strain (ε_{max}) increases with applied cycles for five different loading sequences. For the loading sequence of Case I (σ_{max} = 200 MPa), the TMF peak strain increases from ε_{max} = 0.08 % at the first applied cycle to ε_{max} = 0.092 % at the 10 000th applied cycle; for the loading sequence of Case II (σ_{max1} = 150 MPa and σ_{max2} = 200 MPa), the TMF peak strain increases from ε_{max} = 0.082 % at the first applied cycle to ε_{max} = 0.092 % at the 10 000th applied cycle; for the loading sequence of Case III (σ_{max1} = 180 MPa and σ_{max2} =200 MPa), the TMF peak strain increases from ε_{max} = 0.084 % at the first applied cycle to ε_{max} = 0.092 % at the 10 000th applied cycle; for the loading sequence of Case IV (σ_{max1} = 220 MPa and σ_{max2} = 200 MPa), the TMF peak strain increases from ε_{max} = 0.087 % at the first applied cycle to ε_{max} = 0.092 % at the 10 000th applied cycle; and for the loading sequence of Case V (σ_{max1} = 250 MPa and σ_{max2} = 200 MPa), the TMF peak strain increases from ε_{max} = 0.089 % at the first applied cycle to ε_{max} = 0.092 % at the 10 000th applied cycle, as shown in Fig. 4(c).

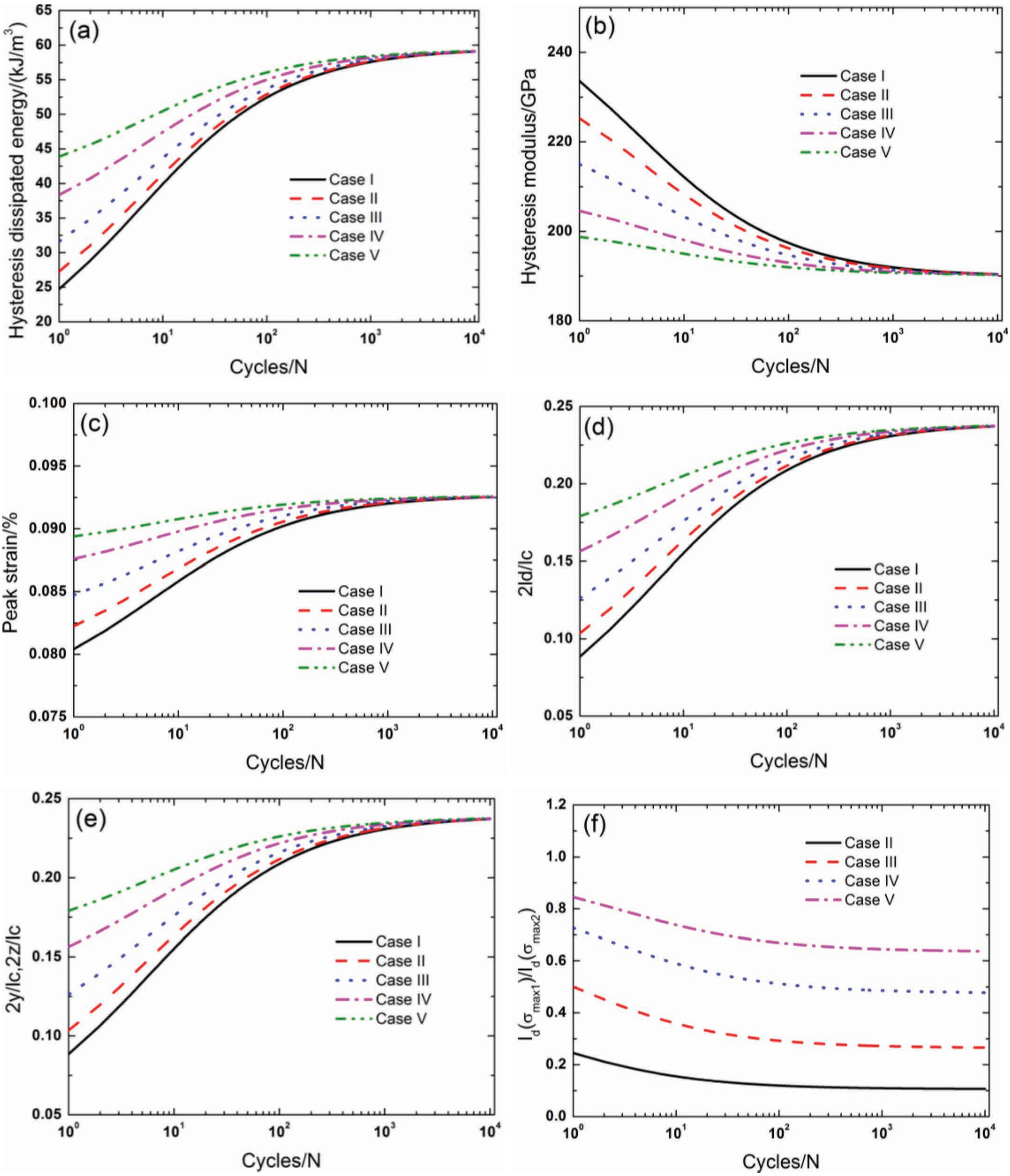

Fig. 4: The damage evolution of SiC/SiC composite under thermomechanical fatigue loading with phase angle of $\theta = \pi/2$ and five different loading modes (Case I: $\sigma_{max} = 200$ MPa; Case II: $\sigma_{max1} = 150$ MPa and $\sigma_{max2} = 200$ MPa; Case III: $\sigma_{max1} = 180$ MPa and $\sigma_{max2} = 200$ MPa; Case IV: $\sigma_{max1} = 220$ MPa and $\sigma_{max2} = 200$ MPa; Case V: $\sigma_{max1} = 250$ MPa and $\sigma_{max2} = 200$ MPa) corresponding to (a) the TMF hysteresis dissipated energy versus cycle number curves; (b) the TMF hysteresis modulus versus cycle number curves; (c) the TMF peak strain versus cycle number curves; (d) the fiber/matrix interface debonding length ($2l_d/l_c$) versus cycle number curves; (e) the fiber/matrix interface sliding length ($2y/l_c$) versus cycle number curves; and (f) the fiber/matrix interface debonding ratio ($l_d(\sigma_{max1})/l_d(\sigma_{max2})$) for different peak stress versus cycle number curves.

Table 3: The TMF damage evolution of SiC/SiC composite at the phase angle of θ = π/2 for different loading sequences.

θ = π/2	Case I		Case II		Case III		Case IV		Case V	
	N = 1	N = 10 000	N = 1	N = 10 000	N = 1	N = 10 000	N = 1	N = 10 000	N = 1	N = 10 000
U_e/(kJ/m^3)	24.7	59	27.2	59	31.6	59	38.3	59	43.8	59
E/(GPa)	233.6	190.3	225.2	190.3	215	190.3	204.5	190.3	198.7	190.3
ε_{max}/(%)	0.08	0.092	0.082	0.092	0.084	0.092	0.087	0.092	0.089	0.092
$2l_d/l_c$	0.088	0.237	0.103	0.237	0.126	0.237	0.156	0.237	0.179	0.237
$2y/l_c$	0.088	0.237	0.103	0.237	0.126	0.237	0.156	0.237	0.179	0.237
$l_d(\sigma_{max1})/l_d(\sigma_{max2})$	–	–	0.244	0.106	0.5	0.26	0.72	0.47	0.84	0.63

The fiber/matrix interface debonding length ($2l_d/l_c$) increases with applied cycles for five different loading sequences. For the loading sequence of Case I (σ_{max} = 200 MPa), the fiber/matrix interface debonded length increases from $2l_d/l_c$ = 0.088 at the first applied cycle to $2l_d/l_c$ = 0.237 at the 10 000th applied cycle; for the loading sequence of Case II (σ_{max1} = 150 MPa and σ_{max2} = 200 MPa), the fiber/matrix interface debonded length increases from $2l_d/l_c$ = 0.103 at the first applied cycle to $2l_d/l_c$ = 0.237 at the 10 000th applied cycle; for the loading sequence of Case III (σ_{max1} =180 MPa and σ_{max2} = 200 MPa), the fiber/matrix interface debonded length increases from $2l_d/l_c$ = 0.126 at the first applied cycle to $2l_d/l_c$ = 0.237 at the 10 000th applied cycle; for the loading sequence of Case IV (σ_{max1} = 220 MPa and σ_{max2} = 200 MPa), the fiber/matrix interface debonded length increases from $2l_d/l_c$ = 0.156 at the first applied cycle to $2l_d/l_c$ = 0.237 at the 10 000th applied cycle; and for the loading sequence of Case V (σ_{max1} = 250 MPa and σ_{max2} = 200 MPa), the fiber/matrix interface debonded length increases from $2l_d/l_c$ = 0.179 at the first applied cycle to $2l_d/l_c$ = 0.237 at the 10 000th applied cycle, as shown in Fig. 4(d).

The fiber/matrix interface sliding length ($2y/l_c$ and $2z/l_c$) increases with applied cycles for five different loading sequences. For the loading sequence of Case I (σ_{max} =200 MPa), the fiber/matrix interface sliding length increases from $2y/l_c$ = 0.088 at the first applied cycle to $2y/l_c$ = 0.237 at the 10 000th applied cycle; for the loading sequence of Case II (σ_{max1} = 150 MPa and σ_{max2} = 200 MPa), the fiber/matrix interface sliding length increases from $2y/l_c$ = 0.103 at the first applied cycle to $2y/l_c$ = 0.237 at the 10 000th applied cycle; for the loading sequence of Case III (σ_{max1} = 180 MPa and σ_{max2} = 200 MPa), the fiber/matrix interface sliding length increases from $2y/l_c$ = 0.126 at the first applied cycle to $2y/l_c$ = 0.237 at the 10 000th applied cycle; for the loading sequence of Case IV (σ_{max1} = 220 MPa and σ_{max2} = 200 MPa), the fiber/matrix interface sliding length increases from $2y/l_c$ = 0.156 at the first applied cycle to $2y/l_c$ = 0.237 at the 10 000th applied cycle; and for the loading sequence of Case V (σ_{max1} = 250 MPa and σ_{max2} = 200 MPa), the fiber/matrix interface sliding length increases from $2y/l_c$ = 0.179 at the first applied cycle to $2y/l_c$ = 0.237 at the 10 000th applied cycle, as shown in Fig. 4(e).

The fiber/matrix interface debonding ratio ($l_d(\sigma_{max1})/l_d(\sigma_{max2})$) for different peak stress decreases with increasing applied cycle for the multiple loading sequence. For the loading sequence of Case II (σ_{max1} = 150 MPa and σ_{max2} = 200 MPa), the fiber/matrix interface debonding ratio decreases from $l_d(\sigma_{max1})/l_d(\sigma_{max2})$ = 0.244 at the first applied cycle to $l_d(\sigma_{max1})/l_d(\sigma_{max2})$ = 0.106 at the 10 000th applied cycle; for the loading sequence of Case III (σ_{max1} = 180 MPa and σ_{max2} = 200 MPa), the fiber/matrix interface debonding ratio decreases from $l_d(\sigma_{max1})/l_d(\sigma_{max2})$ = 0.5 at the first applied cycle to $l_d(\sigma_{max1})/l_d(\sigma_{max2})$ = 0.26 at the 10 000th applied cycle; for the loading sequence of Case IV (σ_{max1} = 220 MPa and σ_{max2} = 200 MPa), the fiber/matrix interface debonding ratio decreases from $l_d(\sigma_{max1})/l_d(\sigma_{max2})$ = 0.72 at the first applied cycle to $l_d(\sigma_{max1})/l_d(\sigma_{max2})$ = 0.47 at the 10 000th applied cycle; and for the loading sequence of Case V (σ_{max1} =250 MPa and σ_{max2} = 200 MPa), the fiber/matrix interface debonding ratio decreases from $l_d(\sigma_{max1})/l_d(\sigma_{max2})$ = 0.84 at the first applied cycle to $l_d(\sigma_{max1})/l_d(\sigma_{max2})$ = 0.63 at the 10 000th applied cycle, as shown in Fig. 4(f).

(d) $\theta = \pi$

When the phase angle is $\theta = \pi$, the evolution of TMF hysteresis dissipated energy (U_e), hysteresis modulus (E), peak strain (ε_{max}), fiber/matrix interface debonding length ($2l_d/l_c$), fiber/matrix interface sliding length ($2y/l_c$) and fiber/matrix interface debonding ratio ($l_d(\sigma_{max1})/l_d(\sigma_{max2})$) with increasing applied cycles for different loading sequences are shown in Fig. 5 and listed in Table 4.

The TMF hysteresis dissipated energy (U_e) increases with applied cycles for five different loading sequences. For the loading sequence of Case I (σ_{max} =200 MPa), the TMF hysteresis dissipated energy increases from U_e = 7.6 kJ/m^3 at the first applied cycle to U_e = 12.7 kJ/m^3 at the 10 000th applied cycle; for the loading sequence of Case II (σ_{max1} = 150 MPa and σ_{max2} = 200 MPa), the TMF hysteresis dissipated energy increases from U_e = 7.8 kJ/m^3 at the first applied cycle to U_e = 12.7 kJ/m^3 at the 10 000th applied cycle; for the loading sequence of Case III (σ_{max1} = 180 MPa and σ_{max2} = 200 MPa), the TMF hysteresis dissipated energy increases from U_e = 8 kJ/m^3 at the first applied cycle to U_e = 12.7 kJ/m^3 at the 10 000th applied cycle; for the loading sequence of Case IV (σ_{max1} = 220 MPa and σ_{max2} = 200 MPa), the TMF hysteresis dissipated energy

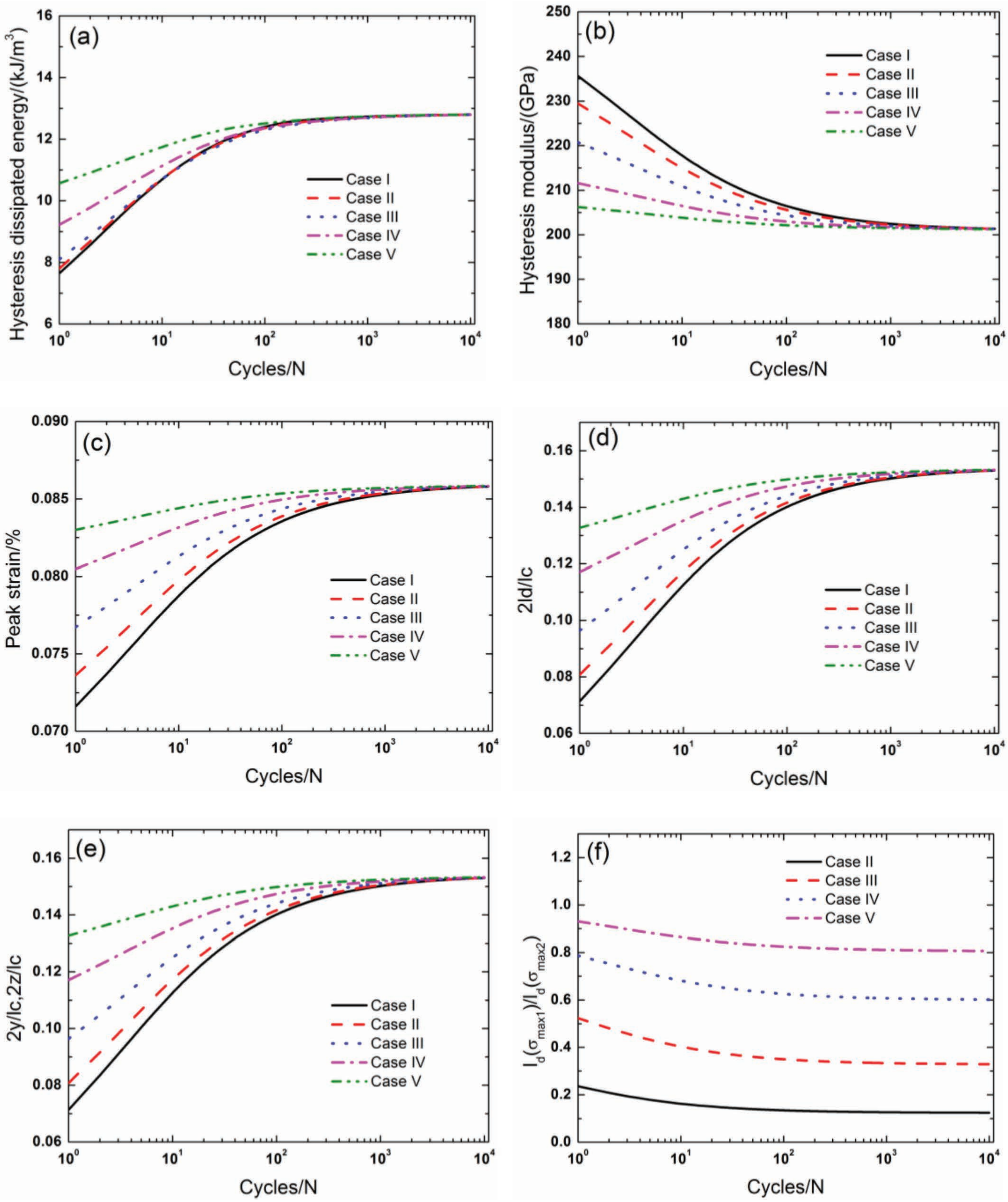

Fig. 5: The damage evolution of SiC/SiC composite under thermomechanical fatigue loading with phase angle of $\theta = \pi$ and five different loading modes (Case I: $\sigma_{max} = 200$ MPa; Case II: $\sigma_{max1} = 150$ MPa and $\sigma_{max2} = 200$ MPa; Case III: $\sigma_{max1} = 180$ MPa and $\sigma_{max2} = 200$ MPa; Case IV: $\sigma_{max1} = 220$ MPa and $\sigma_{max2} = 200$ MPa; Case V: $\sigma_{max1} = 250$ MPa and $\sigma_{max2} = 200$ MPa) corresponding to (a) the TMF hysteresis dissipated energy versus cycle number curves; (b) the TMF hysteresis modulus versus cycle number curves; (c) the TMF peak strain versus cycle number curves; (d) the fiber/matrix interface debonding length ($2l_d/l_c$) versus cycle number curves; (e) the fiber/matrix interface sliding length ($2y/l_c$) versus cycle number curves; and (f) the fiber/matrix interface debonding ratio ($l_d(\sigma_{max1})/l_d(\sigma_{max2})$) for different peak stress versus cycle number curves.

Table 4: The TMF damage evolution of SiC/SiC composite at the phase angle of θ = π for different loading sequences.

θ = π	Case I		Case II		Case III		Case IV		Case V	
	$N = 1$	$N = 10\,000$	$N = 1$	$N = 10\,000$	$N = 1$	$N = 10\,000$	$N = 1$	$N = 10\,000$	$N = 1$	$N = 10\,000$
$U_e/(\mathrm{kJ/m^3})$	7.6	12.7	7.8	12.7	8	12.7	9.2	12.7	10.5	12.7
$E/(\mathrm{GPa})$	235.6	201.3	229.4	201.3	220.7	201.3	211.5	201.3	206.2	201.3
$\varepsilon_{max}/(\%)$	0.071	0.085	0.073	0.085	0.076	0.085	0.08	0.085	0.083	0.085
$2l_d/l_c$	0.071	0.153	0.08	0.153	0.096	0.153	0.117	0.153	0.132	0.153
$2y/l_c$	0.071	0.153	0.08	0.153	0.096	0.153	0.117	0.153	0.132	0.153
$l_d(\sigma_{max1})/l_d(\sigma_{max2})$	–	–	0.235	0.124	0.523	0.329	0.787	0.6	0.93	0.8

increases from $U_e = 9.2\ \mathrm{kJ/m^3}$ at the first applied cycle to $U_e = 12.7\ \mathrm{kJ/m^3}$ at the 10 000th applied cycle; and for the loading sequence of Case V ($\sigma_{max1} = 250$ MPa and $\sigma_{max2} = 200$ MPa), the TMF hysteresis dissipated energy increases from $U_e = 10.5\ \mathrm{kJ/m^3}$ at the first applied cycle to $U_e = 12.7\ \mathrm{kJ/m^3}$ at the 10 000th applied cycle, as shown in Fig. 5(a).

The TMF hysteresis modulus (E) decreases with applied cycles for five different loading sequences. For the loading sequence of Case I ($\sigma_{max} = 200$ MPa), the TMF hysteresis modulus decreases from $E = 235.6$ GPa at the first applied cycle to $E = 201.3$ GPa at the 10 000th applied cycle; for the loading sequence of Case II ($\sigma_{max1} =150$ MPa and $\sigma_{max2} = 200$ MPa), the TMF hysteresis modulus decreases from $E = 229.4$ GPa at the first applied cycle to $E = 201.3$ GPa at the 10 000th applied cycle; for the loading sequence of Case III ($\sigma_{max1} = 180$ MPa and $\sigma_{max2} = 200$ MPa), the TMF hysteresis modulus decreases from $E = 220.7$ GPa at the first applied cycle to $E = 201.3$ GPa at the 10 000th applied cycle; for the loading sequence of Case IV ($\sigma_{max1} = 220$ MPa and $\sigma_{max2} = 200$ MPa), the TMF hysteresis modulus decreases from $E = 211.5$ GPa at the first applied cycle to $E = 201.3$ GPa at the 10 000th applied cycle; and for the loading sequence of Case V ($\sigma_{max1} = 250$ MPa and $\sigma_{max2} = 200$ MPa), the TMF hysteresis modulus decreases from $E = 206.2$ GPa at the first applied cycle to $E = 201.3$ GPa at the 10 000th applied cycle, as shown in Fig. 5(b).

The TMF peak strain (ε_{max}) increases with applied cycles for five different loading sequences. For the loading sequence of Case I ($\sigma_{max} = 200$ MPa), the TMF peak strain increases from $\varepsilon_{max} = 0.071$ % at the first applied cycle to $\varepsilon_{max} = 0.085$ % at the 10 000th applied cycle; for the loading sequence of Case II ($\sigma_{max1} =150$ MPa and $\sigma_{max2} = 200$ MPa), the TMF peak strain increases from $\varepsilon_{max} = 0.073$ % at the first applied cycle to $\varepsilon_{max} = 0.085$ % at the 10 000th applied cycle; for the loading sequence of Case III ($\sigma_{max1} = 180$ MPa and $\sigma_{max2} =200$ MPa), the TMF peak strain increases from $\varepsilon_{max} = 0.076$ % at the first applied cycle to $\varepsilon_{max} = 0.085$ % at the 10 000th applied cycle; for the loading sequence of Case IV ($\sigma_{max1} = 220$ MPa and $\sigma_{max2} = 200$ MPa), the TMF peak strain increases from $\varepsilon_{max} =0.08$ % at the first applied cycle to $\varepsilon_{max} = 0.085$ % at the 10 000th applied cycle; and for the loading sequence of Case V ($\sigma_{max1} = 250$ MPa and $\sigma_{max2} = 200$ MPa), the TMF peak strain increases from $\varepsilon_{max} = 0.083$ % at the first applied cycle to $\varepsilon_{max} = 0.085$ % at the 10 000th applied cycle, as shown in Fig. 5(c).

The fiber/matrix interface debonding length ($2l_d/l_c$) increases with applied cycles for five different loading sequences. For the loading sequence of Case I (σ_{max} =200 MPa), the fiber/matrix interface debonded length increases from $2l_d/l_c = 0.071$ at the first applied cycle to $2l_d/l_c = 0.153$ at the 10 000th applied cycle; for the loading sequence of Case II ($\sigma_{max1} = 150$ MPa and $\sigma_{max2} = 200$ MPa), the fiber/matrix interface debonded length increases from $2l_d/l_c = 0.08$ at the first applied cycle to $2l_d/l_c = 0.153$ at the 10 000th applied cycle; for the loading sequence of Case III ($\sigma_{max1} = 180$ MPa and $\sigma_{max2} = 200$ MPa), the fiber/matrix interface debonded length increases from $2l_d/l_c = 0.096$ at the first applied cycle to $2l_d/l_c = 0.153$ at the 10 000th applied cycle; for the loading sequence of Case IV ($\sigma_{max1} = 220$ MPa and $\sigma_{max2} = 200$ MPa), the fiber/matrix interface debonded length increases from $2l_d/l_c = 0.117$ at the first applied cycle to $2l_d/l_c = 0.153$ at the 10 000th applied cycle; and for the loading sequence of Case V ($\sigma_{max1} = 250$ MPa and $\sigma_{max2} = 200$ MPa), the fiber/matrix interface debonded length increases from $2l_d/l_c = 0.132$ at the first applied cycle to $2l_d/l_c = 0.153$ at the 10 000th applied cycle, as shown in Fig. 5(d).

The fiber/matrix interface sliding length ($2y/l_c$ and $2z/l_c$) increases with applied cycles for five different loading sequences. For the loading sequence of Case I ($\sigma_{max} = 200$ MPa), the fiber/matrix interface sliding length increases from $2y/l_c = 0.071$ at the first applied cycle to $2y/l_c = 0.153$ at the 10 000th applied cycle; for the loading sequence of Case II ($\sigma_{max1} = 150$ MPa and $\sigma_{max2} = 200$ MPa), the fiber/matrix interface sliding length increases from $2y/l_c = 0.08$ at the first applied cycle to $2y/l_c = 0.153$ at the 10 000th applied cycle; for the loading sequence of Case III ($\sigma_{max1} = 180$ MPa and $\sigma_{max2} = 200$ MPa), the fiber/matrix interface sliding length increases from $2y/l_c = 0.096$ at the first applied cycle to $2y/l_c = 0.153$ at the 10 000th applied cycle; for the loading sequence of Case IV ($\sigma_{max1} = 220$ MPa and $\sigma_{max2} = 200$ MPa), the fiber/matrix interface sliding length increases from $2y/l_c = 0.117$ at the first applied cycle to $2y/l_c = 0.153$ at the 10 000th applied cycle; and for the loading sequence of Case V ($\sigma_{max1} = 250$ MPa and $\sigma_{max2} = 200$ MPa), the fiber/matrix interface sliding length increases from $2y/l_c = 0.132$ at the first applied cycle to $2y/l_c = 0.153$ at the 10 000th applied cycle, as shown in Fig. 5(e).

The fiber/matrix interface debonding ratio ($l_d(\sigma_{max1})/l_d(\sigma_{max2})$) for different peak stress decreases with increasing applied cycle for multiple loading sequence. For the loading sequence of Case II ($\sigma_{max1} = 150$ MPa and $\sigma_{max2} = 200$ MPa), the fiber/matrix interface debonding ratio decreases from $l_d(\sigma_{max1})/l_d(\sigma_{max2}) = 0.235$ at the first applied cycle to $l_d(\sigma_{max1})/l_d(\sigma_{max2}) = 0.124$ at the 10 000th applied cycle; for the loading sequence of Case III ($\sigma_{max1} = 180$ MPa and $\sigma_{max2} = 200$ MPa), the fiber/matrix interface debonding ratio decreases from $l_d(\sigma_{max1})/l_d(\sigma_{max2}) = 0.523$ at the first applied cycle to $l_d(\sigma_{max1})/l_d(\sigma_{max2}) = 0.329$ at the 10 000th applied cycle; for the loading sequence of Case IV ($\sigma_{max1} = 220$ MPa and $\sigma_{max2} = 200$ MPa), the fiber/matrix interface debonding ratio decreases from $l_d(\sigma_{max1})/l_d(\sigma_{max2}) = 0.787$ at the first applied cycle to $l_d(\sigma_{max1})/l_d(\sigma_{max2}) = 0.6$ at the 10 000th applied cycle; and for the loading sequence of Case V ($\sigma_{max1} = 250$ MPa and $\sigma_{max2} = 200$ MPa), the fiber/matrix interface debonding ratio decreases from $l_d(\sigma_{max1})/l_d(\sigma_{max2}) = 0.93$ at the first applied cycle to $l_d(\sigma_{max1})/l_d(\sigma_{max2}) = 0.8$ at the 10 000th applied cycle, as shown in Fig. 5(f).

III. Results and Discussions

Under the TMF multiple loading sequences of Case II ($\sigma_{max1} = 150$ MPa and $\sigma_{max2} = 200$ MPa) and Case V ($\sigma_{max1} = 250$ MPa and $\sigma_{max2} = 200$ MPa), the comparisons of damage evolution of TMF hysteresis dissipated energy, hysteresis modulus and peak strain for different phase angles of $\theta = 0$, $\pi/3$, $\pi/2$ and π are shown in Fig. 6. The steady-state TMF hysteresis dissipated energy is the highest for the phase angle of $\theta = \pi/2$, and the lowest for the phase angle of $\theta = \pi$; the steady-state TMF hysteresis modulus is the highest for the phase angle of $\theta = \pi$, and the lowest for the phase angle of $\theta = 0$; the steady-state TMF peak strain is the highest for the phase angle of $\theta = 0$, and the lowest for the phase angle of $\theta = \pi$; the steady-state fiber/matrix interface debonding/sliding lengths are the highest for the phase angle of $\theta = 0$, and the lowest for the phase angle of $\theta = \pi$; the steady-state fiber/matrix interface debonding ratio is the highest for the phase angle of $\theta = \pi$, and the lowest for the phase angle of $\theta = 0$.

Under the in-phase TMF multiple loading sequence, the effects of fiber volume fraction, matrix crack spacing, fiber/matrix interface debonded energy, stress ratio and thermal cyclic temperature on the damage evolution of SiC/SiC composite are analyzed.

(1) Effect of fiber volume fraction

The effect of fiber volume fraction (i.e. $V_{f-} = 25$ % and 35 %) on the in-phase TMF damage evolution of hysteresis dissipated energy, hysteresis modulus, peak strain, fiber/matrix interface debonding/sliding lengths and fiber/matrix interface debonding ratio for SiC/SiC composite subjected to different loading sequences (i.e. Case I, II, III, IV and V) is shown in Fig. 7.

With increasing fiber volume fraction from $V_f = 25$ % to 35 %, the steady-state in-phase TMF hysteresis dissipated energy decreases from $U_e = 54$ kJ/m^3 to $U_e = 12.5$ kJ/m^3; the steady-state in-phase TMF hysteresis modulus increases from $E = 91.3$ GPa to $E = 153.8$ GPa; the steady-state in-phase TMF peak strain decreases from $\varepsilon_{max} = 0.22$ % to $\varepsilon_{max} = 0.11$ %; the steady-state fiber/matrix interface debonding length decreases from $2l_d/l_c = 0.82$ to $2l_d/l_c = 0.27$; the steady-state fiber/matrix interface sliding length decreases from $2y/l_c = 0.54$ to $2y/l_c = 0.26$; and the steady-state fiber/matrix interface debonding ratio decreases corresponding to the different loading sequences.

(2) Effect of matrix crack spacing

The effect of matrix crack spacing (i.e. $l_c = 100$ and 200 μm) on the in-phase TMF damage evolution hysteresis dissipated energy, hysteresis modulus, peak strain, fiber/matrix interface debonding/sliding lengths and fiber/matrix interface debonding ratio for SiC/SiC composite subjected to different loading sequences (i.e. Case I, II, III, IV and V) is shown in Fig. 8.

With increasing matrix crack spacing from $l_c = 100$ to 200 μm, the steady-state in-phase TMF hysteresis dissipated energy decreases from $U_e = 74.6$ kJ/m^3 to $U_e = 39.2$ kJ/m^3; the steady-state in-phase TMF hysteresis modulus increases from $E = 66$ GPa to $E = 92.3$ GPa; the steady-state in-phase TMF peak strain decreases from $\varepsilon_{max} = 0.23$ % to $\varepsilon_{max} = 0.185$ %; the steady-state fiber/matrix interface debonding length decreases from $2l_d/l_c = 1.0$ to $2l_d/l_c = 0.74$; the steady-state fiber/matrix interface sliding length decreases from $2y/l_c = 1.0$ to $2y/l_c = 0.57$; and the steady-state fiber/matrix interface debonding ratio decreases corresponding to the different loading sequences.

(3) Effect of fiber/matrix interface debonded energy

The effects of fiber/matrix interface debonded energy (i.e. $\zeta_d = 1.5$ and 2.0 J/m^2) on the in-phase TMF damage evolution hysteresis dissipated energy, hysteresis modulus, peak strain, fiber/matrix interface debonding/sliding lengths and fiber/matrix interface debonding ratio for SiC/SiC composite subjected to different loading sequences (i.e. Case I, II, III, IV and V) are shown in Fig. 9.

With increasing fiber/matrix interface debonded energy from $\zeta_d = 1.5$ to 2.0 J/m^2, the steady-state in-phase TMF hysteresis dissipated energy decreases from $U_e = 42.6$ kJ/m^3 to $U_e = 34$ kJ/m^3; the steady-state in-phase TMF hysteresis modulus increases from $E = 95.6$ GPa to $E = 102.7$ GPa; the steady-state in-phase TMF peak strain decreases from $\varepsilon_{max} = 0.197$ % to $\varepsilon_{max} = 0.175$ %; the steady-state fiber/matrix interface debonding length decreases from $2l_d/l_c = 0.64$ to $2l_d/l_c = 0.49$; the steady-state fiber/matrix interface sliding length decreases from $2y/l_c = 0.48$ to $2y/l_c = 0.43$; and the steady-state fiber/matrix interface debonding ratio decreases corresponding to the different loading sequences.

(4) Effects of stress ratio

The effects of the stress ratio (i.e. $R = 0.1$ and 0.5) on the in-phase TMF damage evolution of hysteresis dissipated energy, hysteresis modulus and fiber/matrix interface sliding length for SiC/SiC composite subjected to different loading sequences (i.e. Case I, II, III, IV and V) are shown in Fig. 10.

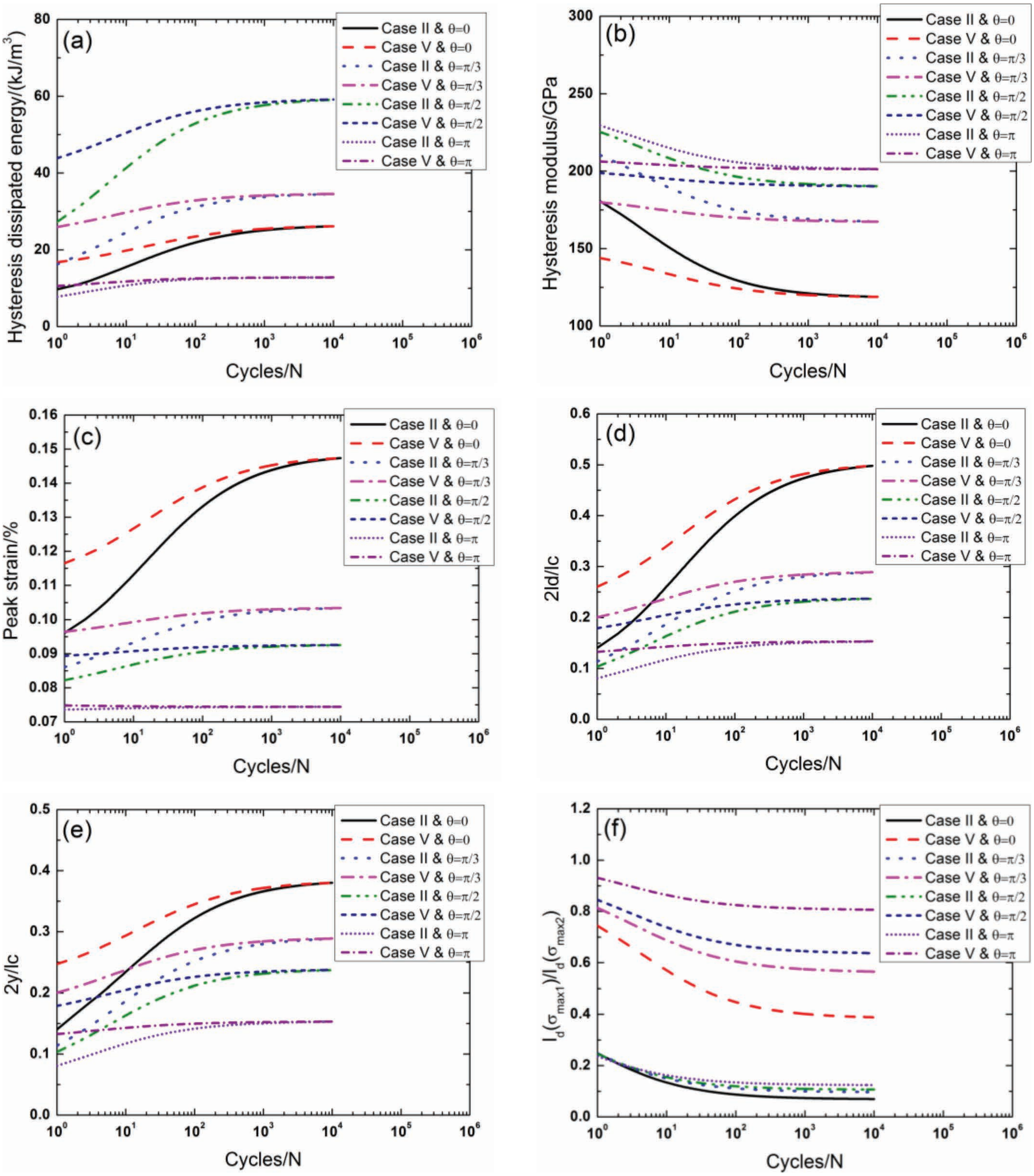

Fig. 6: The comparisons of the damage evolution in SiC/SiC composite under thermomechanical fatigue loading with phase angle of $\theta = 0$, $\pi/3$, $\pi/2$ and π, and two different loading modes (Case II: $\sigma_{max1} = 150$ MPa and $\sigma_{max2} = 200$ MPa; and Case V: $\sigma_{max1} = 250$ MPa and $\sigma_{max2} = 200$ MPa) corresponding to (a) the TMF hysteresis dissipated energy versus cycle number curves; (b) the TMF hysteresis modulus versus cycle number curves; (c) the TMF peak strain versus cycle number curves; (d) the fiber/matrix interface debonding length ($2l_d/l_c$) versus cycle number curves; (e) the fiber/matrix interface sliding length ($2y/l_c$) versus cycle number curves; and (f) the fiber/matrix interface debonding ratio ($l_d(\sigma_{max1})/l_d(\sigma_{max2})$) for different peak stress versus cycle number curves.

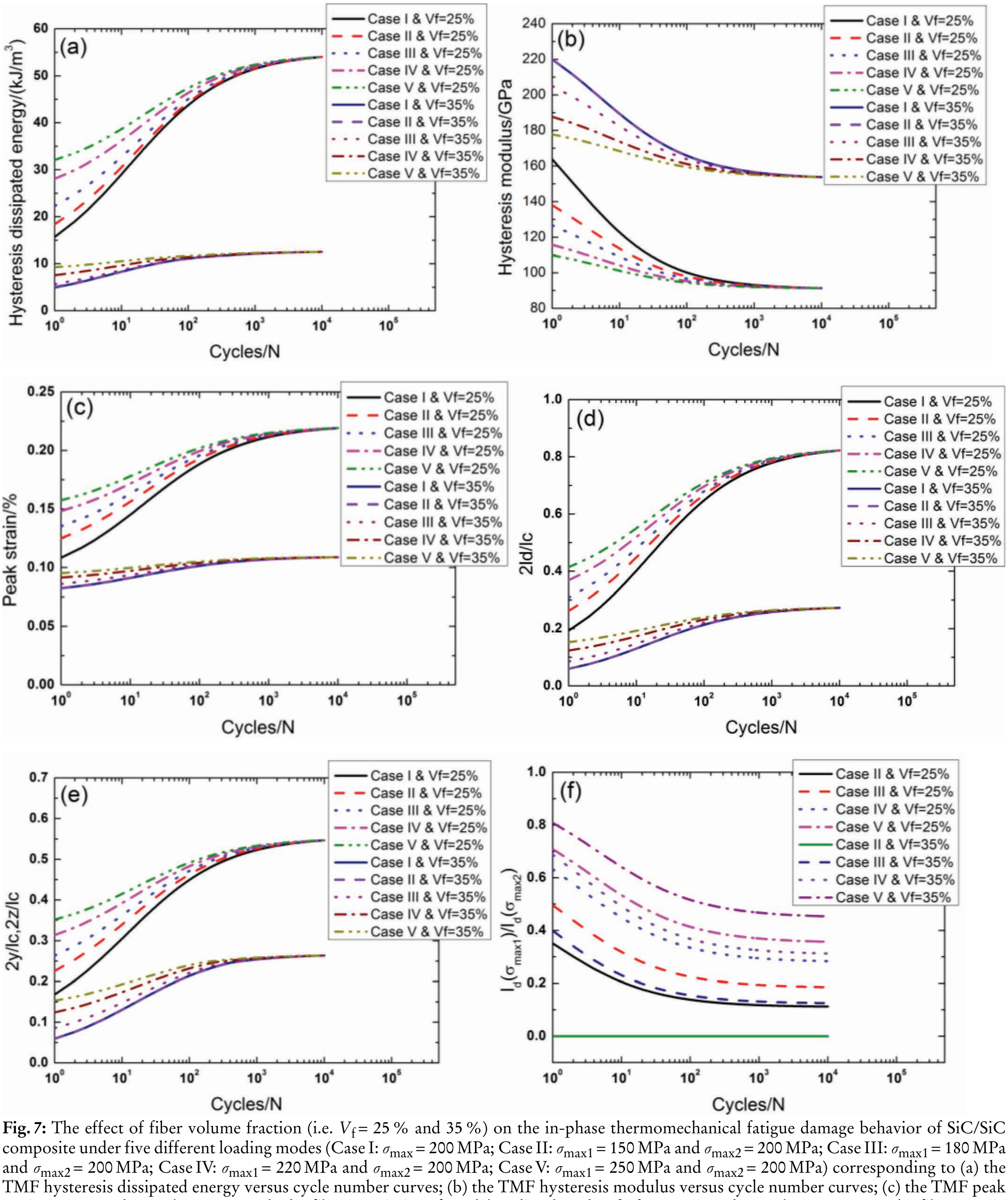

Fig. 7: The effect of fiber volume fraction (i.e. $V_f = 25\,\%$ and $35\,\%$) on the in-phase thermomechanical fatigue damage behavior of SiC/SiC composite under five different loading modes (Case I: $\sigma_{max} = 200$ MPa; Case II: $\sigma_{max1} = 150$ MPa and $\sigma_{max2} = 200$ MPa; Case III: $\sigma_{max1} = 180$ MPa and $\sigma_{max2} = 200$ MPa; Case IV: $\sigma_{max1} = 220$ MPa and $\sigma_{max2} = 200$ MPa; Case V: $\sigma_{max1} = 250$ MPa and $\sigma_{max2} = 200$ MPa) corresponding to (a) the TMF hysteresis dissipated energy versus cycle number curves; (b) the TMF hysteresis modulus versus cycle number curves; (c) the TMF peak strain versus cycle number curves; (d) the fiber/matrix interface debonding length ($2l_d/l_c$) versus cycle number curves; (e) the fiber/matrix interface sliding length ($2y/l_c$) versus cycle number curves; and (f) the fiber/matrix interface debonding ratio ($l_d(\sigma_{max1})/l_d(\sigma_{max2})$) for different peak stress versus cycle number curves.

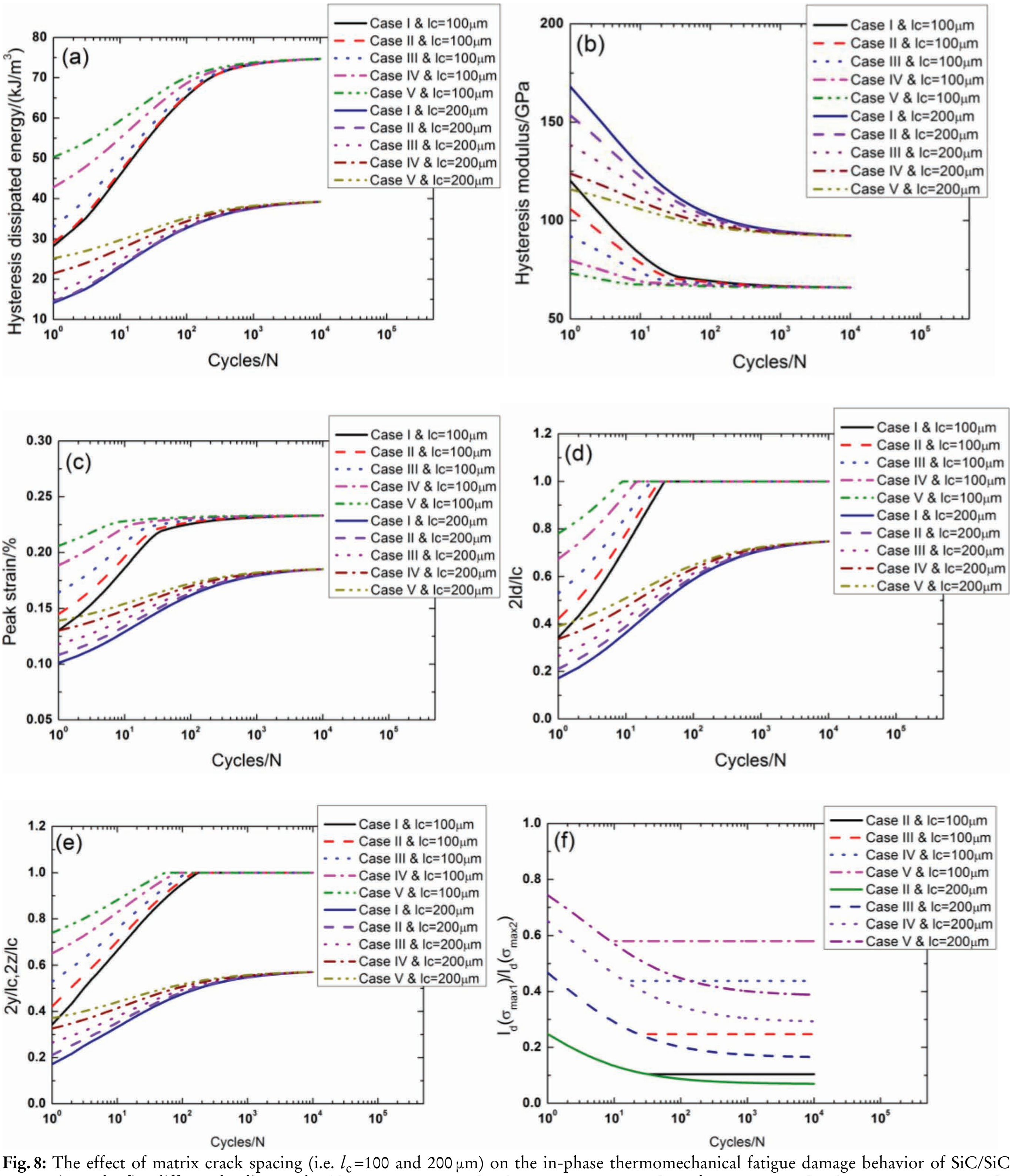

Fig. 8: The effect of matrix crack spacing (i.e. l_c=100 and 200 μm) on the in-phase thermomechanical fatigue damage behavior of SiC/SiC composite under five different loading modes (Case I: σ_{max} = 200 MPa; Case II: σ_{max1} = 150 MPa and σ_{max2} = 200 MPa; Case III: σ_{max1} = 180 MPa and σ_{max2}=200 MPa; Case IV: σ_{max1} = 220 MPa and σ_{max2} = 200 MPa; Case V: σ_{max1} = 250 MPa and σ_{max2} = 200 MPa) corresponding to (a) the TMF hysteresis dissipated energy versus cycle number curves; (b) the TMF hysteresis modulus versus cycle number curves; (c) the TMF peak strain versus cycle number curves; (d) the fiber/matrix interface debonding length ($2l_d/l_c$) versus cycle number curves; (e) the fiber/matrix interface sliding length ($2y/l_c$) versus cycle number curves; and (f) the fiber/matrix interface debonding ratio ($l_d(\sigma_{max1})/l_d(\sigma_{max2})$) for different peak stress versus cycle number curves.

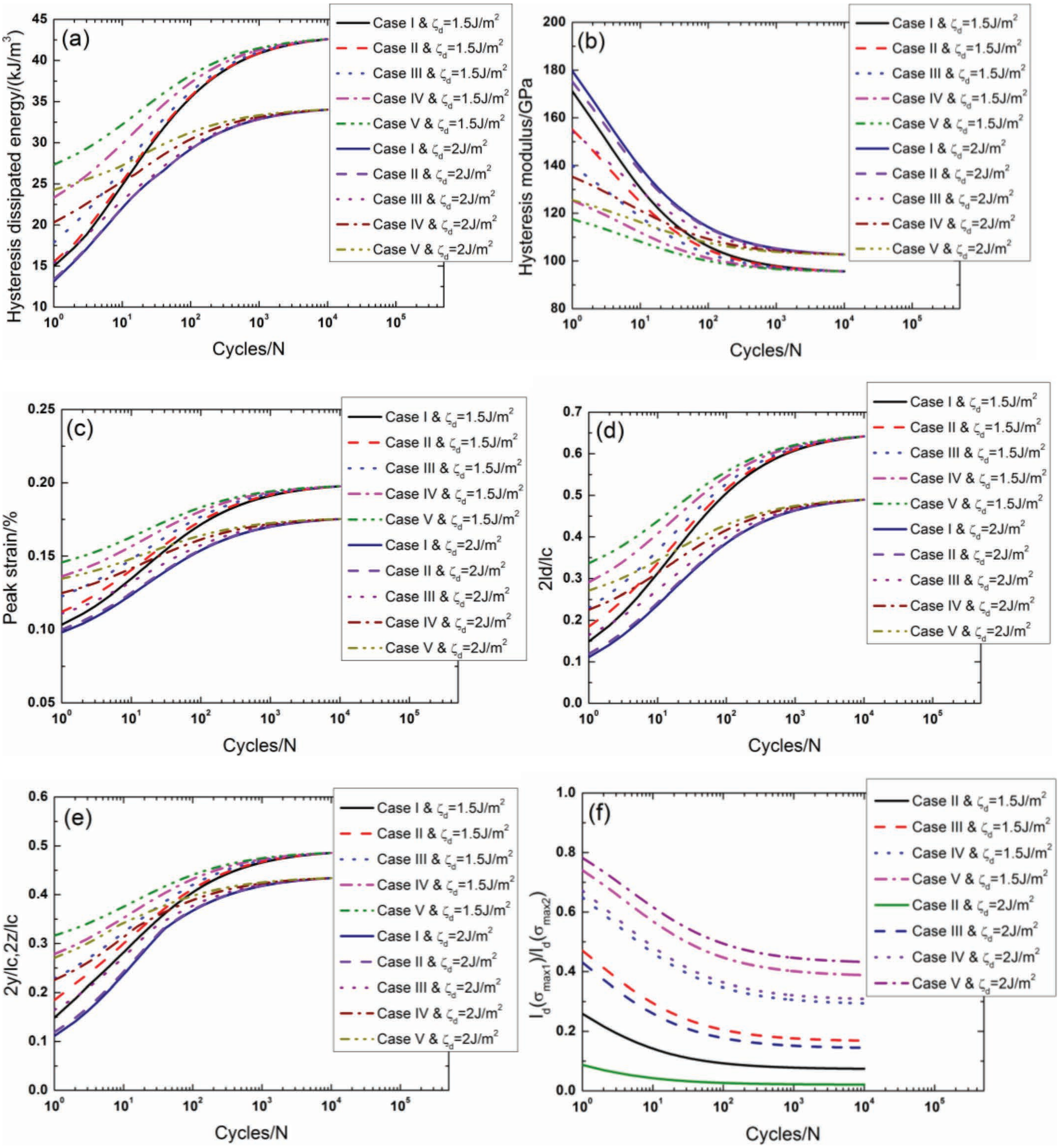

Fig. 9: The effect of fiber/matrix interface debonded energy (i.e. ζ_d = 1.5 and 2 J/m^2) on the in-phase thermomechanical fatigue damage behavior of SiC/SiC composite under five different loading modes (Case I: σ_{max} = 200 MPa; Case II: σ_{max1} = 150 MPa and σ_{max2} = 200 MPa; Case III: σ_{max1} = 180 MPa and σ_{max2} = 200 MPa; Case IV: σ_{max1} = 220 MPa and σ_{max2} = 200 MPa; Case V: σ_{max1} = 250 MPa and σ_{max2} = 200 MPa) corresponding to (a) the TMF hysteresis dissipated energy versus cycle number curves; (b) the TMF hysteresis modulus versus cycle number curves; (c) the TMF peak strain versus cycle number curves; (d) the fiber/matrix interface debonding length ($2l_d/l_c$) versus cycle number curves; (e) the fiber/matrix interface sliding length ($2y/l_c$) versus cycle number curves; and (f) the fiber/matrix interface debonding ratio ($l_d(\sigma_{max1})/l_d(\sigma_{max2})$) for different peak stress versus cycle number curves.

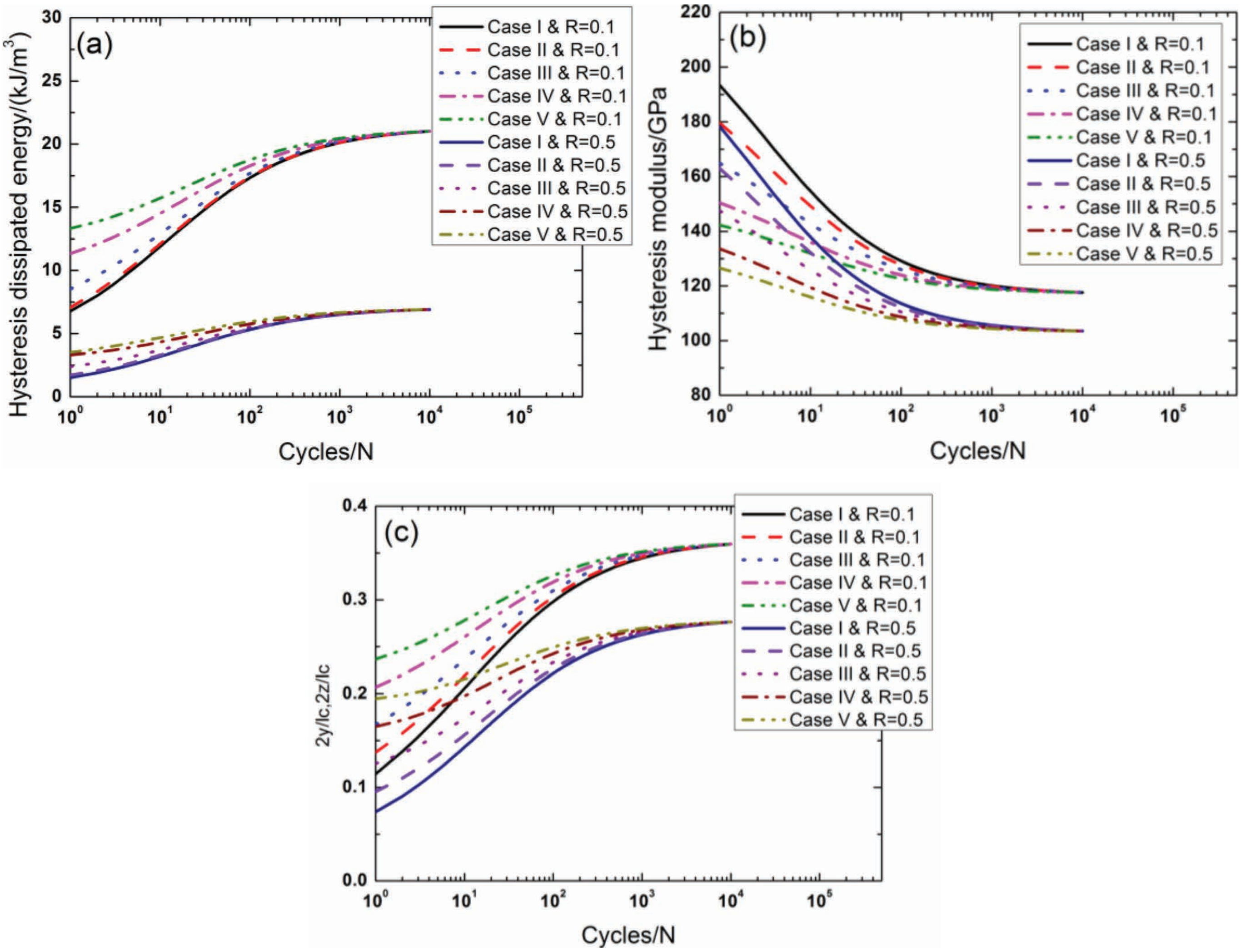

Fig. 10: The effect of stress ratio (i.e. R = 0.1 and 0.5) on the in-phase thermomechanical fatigue damage behavior of SiC/SiC composite under five different loading modes (Case I: σ_{max} = 200 MPa; Case II: σ_{max1} = 150 MPa and σ_{max2} = 200 MPa; Case III: σ_{max1} = 180 MPa and σ_{max2} = 200 MPa; Case IV: σ_{max1} = 220 MPa and σ_{max2} = 200 MPa; Case V: σ_{max1} = 250 MPa and σ_{max2} = 200 MPa) corresponding to (a) the TMF hysteresis dissipated energy versus cycle number curves; (b) the TMF hysteresis modulus versus cycle number curves; and (c) the fiber/matrix interface sliding length ($2y/l_c$) versus cycle number curves.

With increasing stress ratio from R = 0.1 to 0.5, the steady-state in-phase TMF hysteresis dissipated energy decreases from U_e = 21 kJ/m^3 to U_e = 6.9 kJ/m^3; the steady-state in-phase TMF hysteresis modulus decreases from E = 117.5 GPa to E = 103.4 GPa; the steady-state fiber/matrix interface sliding length decreases from $2y/l_c$ = 0.36 to $2y/l_c$ = 0.27.

(5) Effects of thermal cyclic temperature

The effects of thermal cyclic temperature (i.e. T_2 = 500 °C and 800 °C) on the in-phase TMF damage evolution hysteresis dissipated energy, hysteresis modulus, peak strain, fiber/matrix interface debonding/sliding lengths and fiber/matrix interface debonding ratio for SiC/SiC composite subjected to different loading sequences (i.e. Case I, II, III, IV and V) are shown in Fig. 11.

With increasing thermal cyclic temperature from T_2 = 500 °C to T_2 = 800 °C, the steady-state in-phase TMF hysteresis dissipated energy increases from U_e = 17.5 kJ/m^3 to U_e = 20.6 kJ/m^3; the steady-state in-phase TMF hysteresis modulus decreases from E = 177.6 GPa to E = 145.1 GPa; the steady-state in-phase TMF peak strain increases from ε_{max} = 0.089 % to ε_{max} = 0.113 %; the steady-state fiber/matrix interface debonding length increases from $2l_d/l_c$ = 0.22 to $2l_d/l_c$ = 0.33; the steady-state fiber/matrix interface sliding length increases from $2y/l_c$ = 0.22 to $2y/l_c$ = 0.3; and the steady-state fiber/matrix interface debonding ratio decreases corresponding to the different loading sequences.

IV. Experimental Comparisons

The experimental TMF damage evolution of 2D SiC/SiC and cross-ply SiC/MAS composites is predicted using the present analysis.

(1) 2D SiC/SiC composite at 1300 °C in air conditions

Zhu *et al.* [36] investigated the tension–tension fatigue behavior of 2D SiC/SiC composite at 1 300 °C in air conditions. The fatigue tests were performed under the load control with a loading frequency of 20 Hz. The fatigue load ratio was defined to be 0.1. The composite tensile strength was approximately 232 MPa.

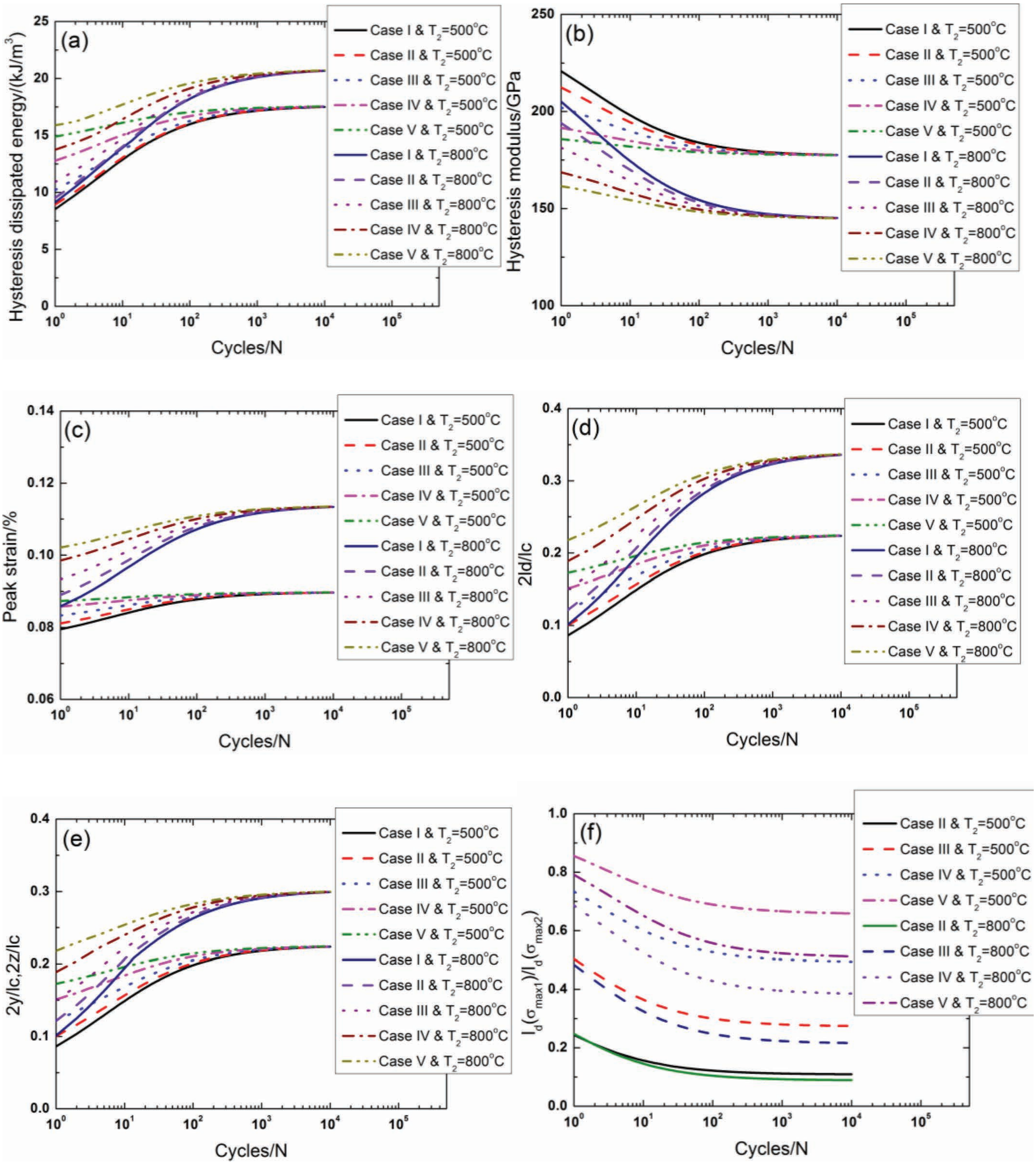

Fig. 11: The effect of thermal cyclic temperature (i.e. $T_2 = 500$ °C and 800 °C) on the in-phase thermomechanical fatigue damage behavior of SiC/SiC composite under five different loading modes (Case I: $\sigma_{max} = 200$ MPa; Case II: $\sigma_{max1} = 150$ MPa and $\sigma_{max2} = 200$ MPa; Case III: $\sigma_{max1} = 180$ MPa and $\sigma_{max2} = 200$ MPa; Case IV: $\sigma_{max1} = 220$ MPa and $\sigma_{max2} = 200$ MPa; Case V: $\sigma_{max1} = 250$ MPa and $\sigma_{max2} = 200$ MPa) corresponding to (a) the TMF hysteresis dissipated energy versus cycle number curves; (b) the TMF hysteresis modulus versus cycle number curves; (c) the TMF peak strain versus cycle number curves; (d) the fiber/matrix interface debonding length ($2l_d/l_c$) versus cycle number curves; (e) the fiber/matrix interface sliding length ($2y/l_c$) versus cycle number curves; and (f) the fiber/matrix interface debonding ratio ($l_d(\sigma_{max1})/l_d(\sigma_{max2})$) for different peak stress versus cycle number curves.

At 1 300 °C in air atmosphere, when the fatigue peak stress is σ_{max} = 90 MPa, the experimental fatigue hysteresis dissipated energy increases with applied cycle number, i.e. from 2.0 kJ/m^3 at the 6 000th applied cycle to 7.8 kJ/m^3 at the 2 800 000th applied cycle, as shown in Fig. 12(a). The fiber/matrix interface shear stress decreases with applied cycle number, i.e. from 12 MPa at the 6 000th applied cycle to 3 MPa at the 2 800 000th applied cycle, as shown in Fig. 12(b). When the fatigue peak stress is σ_{max} = 120 MPa, the experimental fatigue hysteresis dissipated energy increases from 4 kJ/m^3 at the 100th applied cycle to 19 kJ/m^3 at the 36 000th applied cycle, as shown in Fig. 12(a). The fiber/matrix interface shear stress decreases from 18 MPa at the 100th applied cycle to 3.7 MPa at the 36 000th applied cycle, as shown in Fig. 12(b).

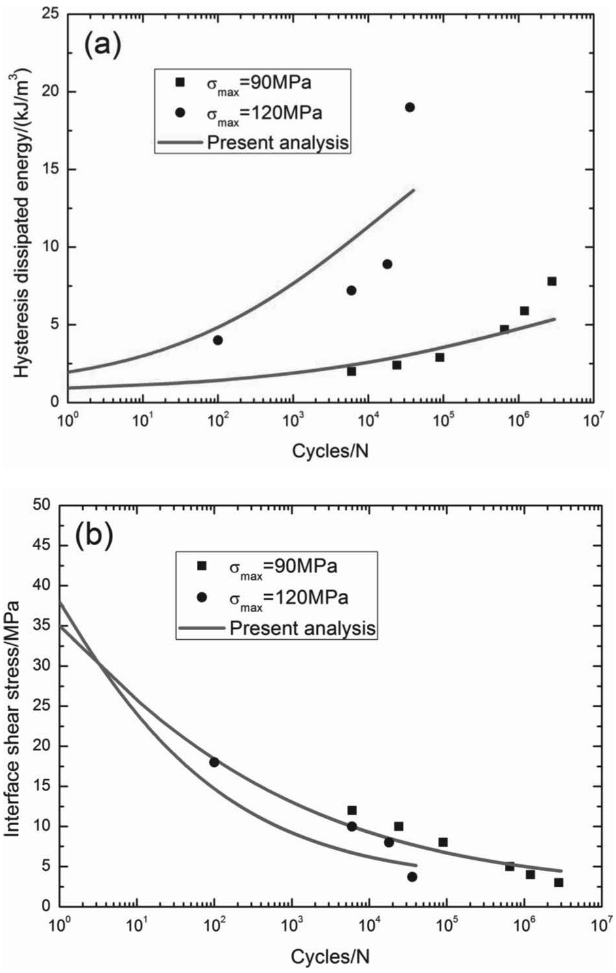

Fig. 12: (a) The experimental and theoretical fatigue hysteresis dissipated energy versus cycle number curves; and (b) the experimental and theoretical interface shear stress versus cycle number curves of 2D SiC/SiC composite at 1300 °C in air.

(2) Cross-ply SiC/MAS composite at 566 °C in air conditions

Steiner [37] investigated the tension–tension fatigue behavior of cross-ply SiC/MAS composite at 566 °C in air conditions. The fatigue tests were performed under load control at a triangular waveform with the loading frequency of 1 and 10 Hz and the fatigue load ratio, i.e. minimum to maximum stress, of 0.1, and the maximum number of applied cycles was defined to be 1 000 000 applied cycles. The tensile strength of cross-ply SiC/MAS composite at 566 °C in air conditions was 292 MPa. The fatigue peak stresses were 137 MPa (47.1 %σ_{UTS}), 120 MPa (41.2 %σ_{UTS}), 103 MPa (35.3%σ_{UTS}), 98 MPa (33.6%σ_{UTS}) and 86 MPa (29.4%σ_{UTS}) at the loading frequency of 10 Hz, and 137 MPa (47.1 %σ_{UTS}), 120 MPa (41.2 %σ_{UTS}), 103 MPa (35.3 %σ_{UTS}), and 99 MPa (34.2 %σ_{UTS}) at the loading frequency of 1 Hz.

At the loading frequency of 1 Hz, when the fatigue peak stress is σ_{max} = 137 MPa, the experimental and theoretical fatigue hysteresis dissipated energy versus the fiber/matrix interface shear stress curves are shown in Fig. 13(a). The theoretical fatigue hysteresis dissipated energy increases with decreasing fiber/matrix interface shear stress from 10.4 kJ/m^3 at τ_i = 20 MPa to the peak values of 20.8 kJ/m^3 at τ_i = 8.2 MPa, and then decreases to 0 kJ/m^3 at τ_i = 0 MPa. The experimental fatigue hysteresis dissipated energy decreases from 5.4 kJ/m^3 at the 4th applied cycle to 4.4 kJ/m^3 at the 230th applied cycle, which lies in the left part of theoretical fatigue hysteresis dissipated energy versus the fiber/matrix interface shear stress curve. The fiber/matrix interface shear stress corresponding to different applied cycle numbers can be obtained from the

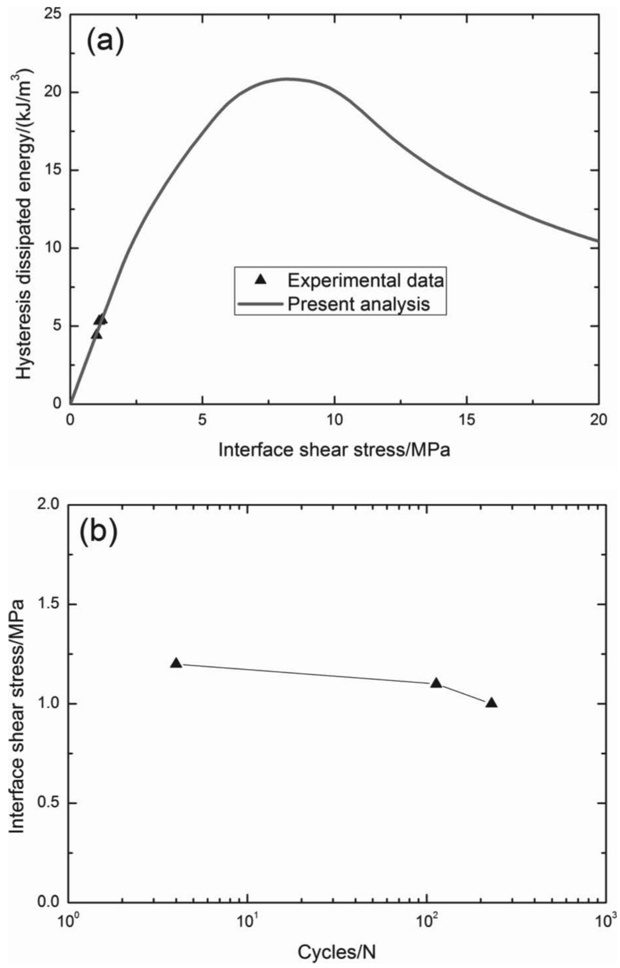

Fig. 13: (a) The experimental and theoretical fatigue hysteresis dissipated energy versus the fiber/matrix interface shear stress curves; and (b) the interface shear stress versus cycle number curve of cross-ply SiC/MAS composite under σ_{max} = 137 MPa and the loading frequency of 1 Hz at 566 °C in air.

fatigue hysteresis dissipated energy, as shown in Fig. 13(b), in which the fiber/matrix interface shear stress decreases from 1.2 MPa at the 4th applied cycle to 1.0 MPa at the 230th applied cycle.

At the loading frequency of 10 Hz, when the fatigue peak stress is σ_{max} = 137 MPa, the experimental fatigue hysteresis dissipated energy decreases from 6.5 kJ/m^3 at the 2nd applied cycle to 3.6 kJ/m^3 at the 7 730th applied cycle, which lies in the left part of the theoretical fatigue hysteresis dissipated energy versus the fiber/matrix interface shear stress curve, as shown in Fig. 14(a). The fiber/matrix interface shear stress corresponding to different applied cycle numbers can be obtained, as shown in Fig. 14(b), in which the fiber/matrix interface shear stress decreases from 1.5 MPa at the 2nd applied cycle to 0.8 MPa at the 7 730th applied cycle.

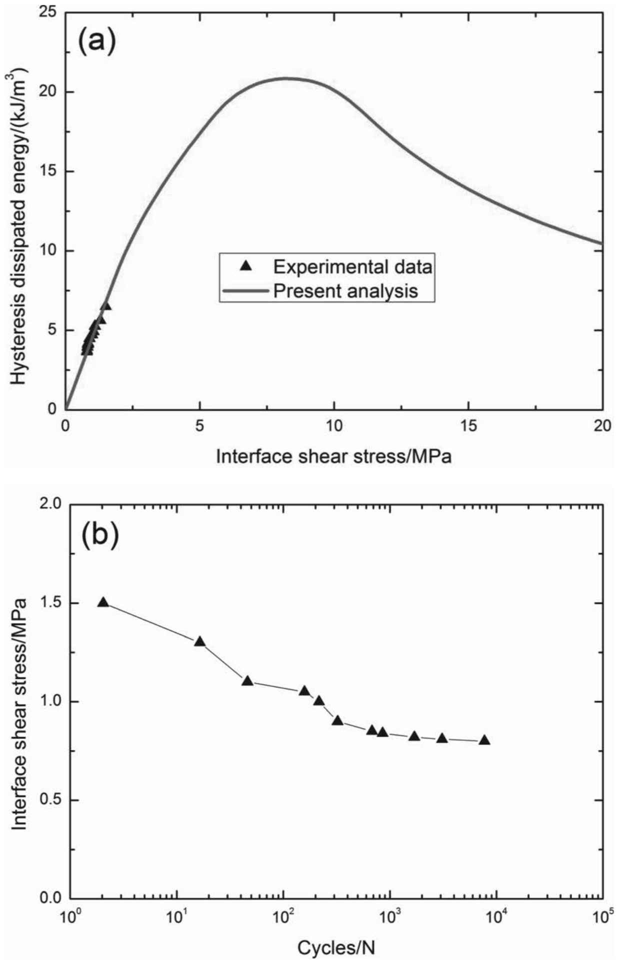

Fig. 14: (a) The experimental and theoretical fatigue hysteresis dissipated energy versus the fiber/matrix interface shear stress curves; and (b) the interface shear stress versus cycle number curve of cross-ply SiC/MAS composite under σ_{max} = 137 MPa and the loading frequency of 10 Hz at 566 °C in air.

(3) Cross-ply SiC/MAS composite at 1 093 °C in air conditions

Steiner [37] investigated the tension–tension fatigue behavior of cross-ply SiC/MAS composite at 1 093 °C in air conditions. The fatigue tests were performed under load control at a triangular waveform with the loading frequency of 1 and 10 Hz and the fatigue load ratio, i.e. minimum to maximum stress, of 0.1, and the maximum number of applied cycles was defined to be 1 000 000 applied cycles. The tensile strength of SiC/MAS at 1 093 °C in air was 209 MPa. The fatigue peak stresses were 137 MPa (65.8 % σ_{UTS}), 103 MPa (49.4 % σ_{UTS}), 96 MPa (46.1 % σ_{UTS}), 94 MPa (45.3 % σ_{UTS}) and 86 MPa (41.1 % σ_{UTS}) at the loading frequency of 10 Hz, and 137 MPa (65.8 % σ_{UTS}), 120 MPa (57.6 % σ_{UTS}), 103 MPa (49.4 % σ_{UTS}), 96 MPa (46.1 % σ_{UTS}), and 86 MPa (41.1 % σ_{UTS}) at the loading frequency of 1 Hz.

At the loading frequency of 1 Hz, when the fatigue peak stress is σ_{max} = 103 MPa, the experimental and theoretical fatigue hysteresis dissipated energy versus the fiber/matrix interface shear stress curves are shown in Fig. 15(a). The theoretical fatigue hysteresis dissipated energy increases with decreasing fiber/matrix interface shear stress from 11.9 kJ/m^3 at τ_i =20 MPa to 25.5 kJ/m^3 at τ_i = 7.8 MPa, and then decreases to 0 kJ/m^3 at τ_i = 0 MPa. The experimental fatigue hysteresis dissipated energydecreases from 25.5 kJ/m^3 at the 4th applied cycle to 6.5 kJ/m^3 at the 10 608th applied cycle, which lies in the left part of theoretical fatigue hysteresis dissipated energy versus the fiber/matrix interface shear stress curve. The fiber/matrix interface shear stress corresponding to

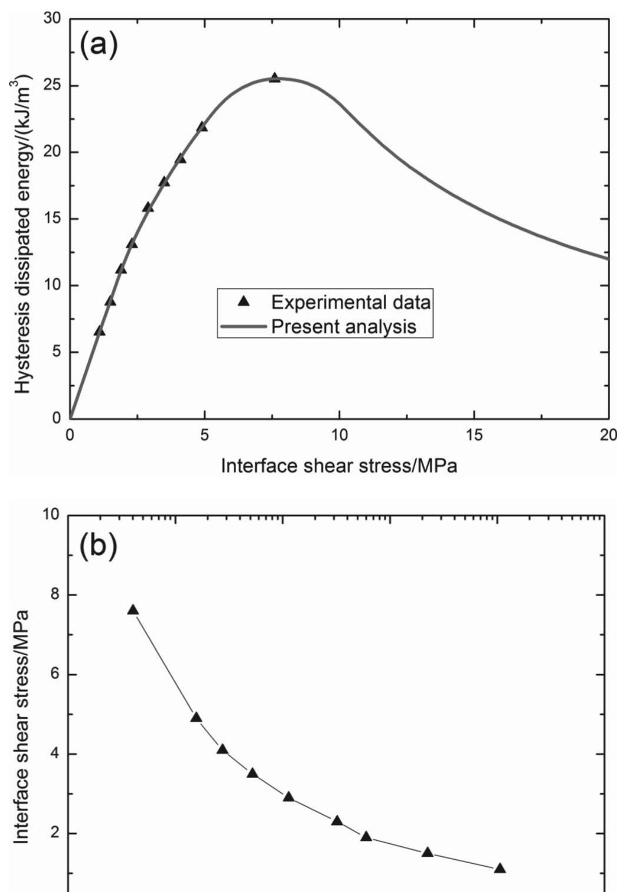

Fig. 15: (a) The experimental and theoretical fatigue hysteresis dissipated energy versus the fiber/matrix interface shear stress curves; and (b) the interface shear stress versus cycle number curve of cross-ply SiC/MAS composite under σ_{max} = 103 MPa and the loading frequency of 1 Hz at 1 093 °C in air.

different applied cycle numbers can be obtained, as shown in Fig. 15(b), in which the fiber/matrix interface shear stress decreases from 7.6 MPa at the 4th applied cycle to 1.1 MPa at the 10 608th applied cycle.

At the loading frequency of 10 Hz, when the fatigue peak stress is σ_{max} = 103 MPa, the experimental fatigue hysteresis dissipated energy decreases from 13 kJ/m^3 at the 6th applied cycle to 3.1 kJ/m^3 at the 94 044th applied cycle, which lies in the left part of the theoretical fatigue hysteresis dissipated energy versus the fiber/matrix interface shear stress curve, as shown in Fig. 16(a). The fiber/matrix interface shear stress corresponding to different applied cycle numbers can be obtained, as shown in Fig. 16(b), in which the fiber/matrix interface shear stress decreases from 2.4 MPa at the 6th applied cycle to 0.6 MPa at the 94 044th applied cycle.

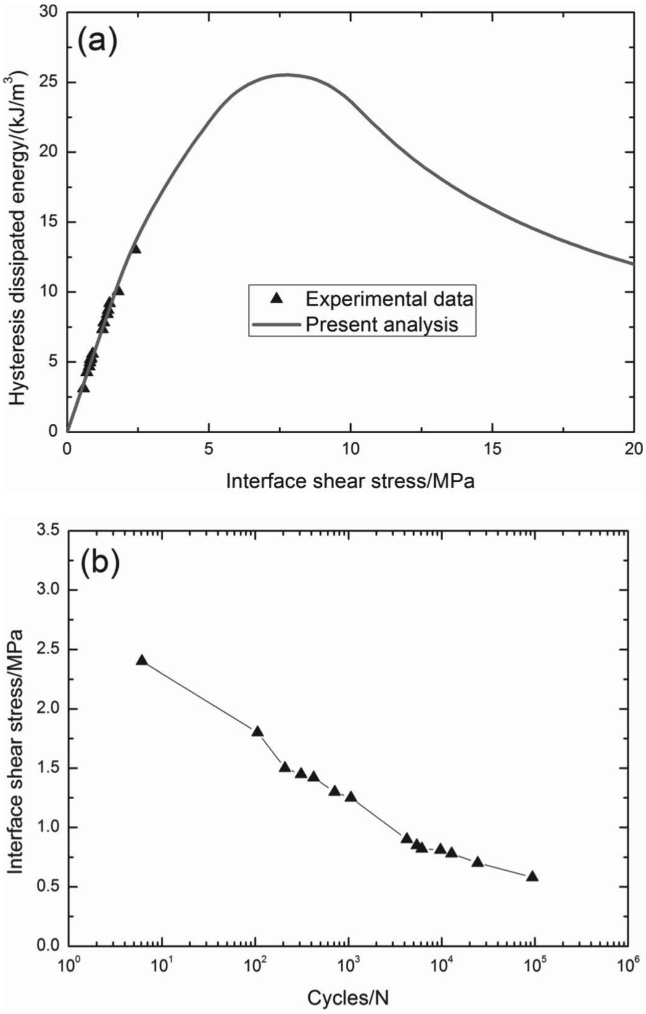

Fig. 16: (a) The experimental and theoretical fatigue hysteresis dissipated energy versus interface shear stress curves; and (b) the interface shear stress versus cycle number curve of cross-ply SiC/MAS composite under σ_{max} = 103 MPa and the loading frequency of 10 Hz at 1 093 °C in air.

(4) Cross-ply SiC/MAS composite under in-phase TMF loading

Allen and Mall [38] investigated the in-phase TMF loading behavior of cross-ply SiC/MAS composite at the thermal cyclic temperature range of 566 °C and 1093 °C. The monotonic tensile stress–strain curves of cross-ply SiC/MAS composite at 566 °C and 1093 °C are shown in Fig. 17. At 566 °C, the composite tensile strength is 292 MPa and the failure strain is 0.76 %; and at 1 093 °C, the composite tensile strength is 218 MPa and the failure strain is 0.83 %.

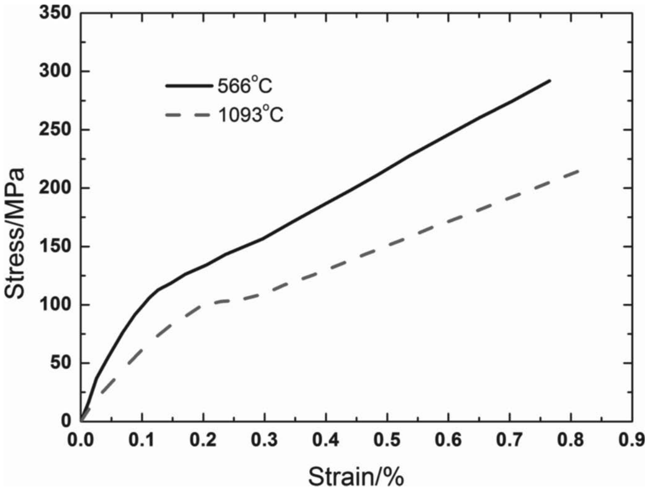

Fig. 17: The tensile stress-strain curves of cross-ply SiC/MAS composite at 566 °C and 1093 °C.

Under TMF constant peak stress of σ_{max} = 85 MPa, the TMF hysteresis dissipated energy increases from $U_e(N = 1)$ = 11.6 kJ/m^3 to $U_e(N = 100)$ = 17.7 kJ/m^3; under the TMF multiple loading sequence of σ_{max1} = 85 MPa and σ_{max2} = 105 MPa, the TMF hysteresis dissipated energy increases to the peak value of $U_e(N = 10)$ = 27.5 kJ/m^3 and then decreases to $U_e(N = 100)$ = 23.9 kJ/m^3; and under the TMF multiple loading sequence of σ_{max1} = 85 MPa, σ_{max2} = 105 MPa and σ_{max3} = 120 MPa, the TMF hysteresis dissipated energy increases to the peak value of $U_e(N = 13)$ = 37.4 kJ/m^3 and then decreases to $U_e(N = 100)$ = 34.5 kJ/m^3, as shown in Fig. 18.

Under TMF constant peak stress of σ_{max} = 85 MPa, the TMF hysteresis modulus decreases from $E(N = 1)$ = 113.5 GPa to $E(N = 100)$ = 92.1 GPa; under the TMF multiple loading sequence of σ_{max1} = 85 MPa and σ_{max2} = 105 MPa, the TMF hysteresis modulus decreases from $E(N = 1)$ = 71.5 GPa to $E(N = 100)$ = 50 GPa; and under the TMF multiple loading sequence of σ_{max1} = 85 MPa, σ_{max2} = 105 MPa and σ_{max3} = 120 MPa, the TMF hysteresis modulus decreases from $E(N = 1)$ = 65.5 GPa to $E(N = 100)$ = 42.5 GPa, as shown in Fig. 19.

Under TMF constant peak stress of σ_{max} = 85 MPa, the TMF peak strain increases from $\varepsilon_{max}(N = 1)$ = 0.147 % to $\varepsilon_{max}(N = 350)$ = 0.214 %, and the fiber/matrix interface debonding length increases from $2l_d/l_c$ = 0.4 at N = 1 to $2l_d/l_c$ = 0.67 at N = 100; and under TMF multiple loading sequence of σ_{max1} = 85 MPa and σ_{max2} = 105 MPa, the TMF peak strain increases from $\varepsilon_{max}(N = 1)$ = 0.227 % to $\varepsilon_{max}(N = 100)$ = 0.274 %, and the fiber/matrix interface debonding length increases from $2l_d/l_c$ = 0.54 at N = 1 to $2l_d/l_c$ = 0.98 at N = 100, as shown in Fig. 20.

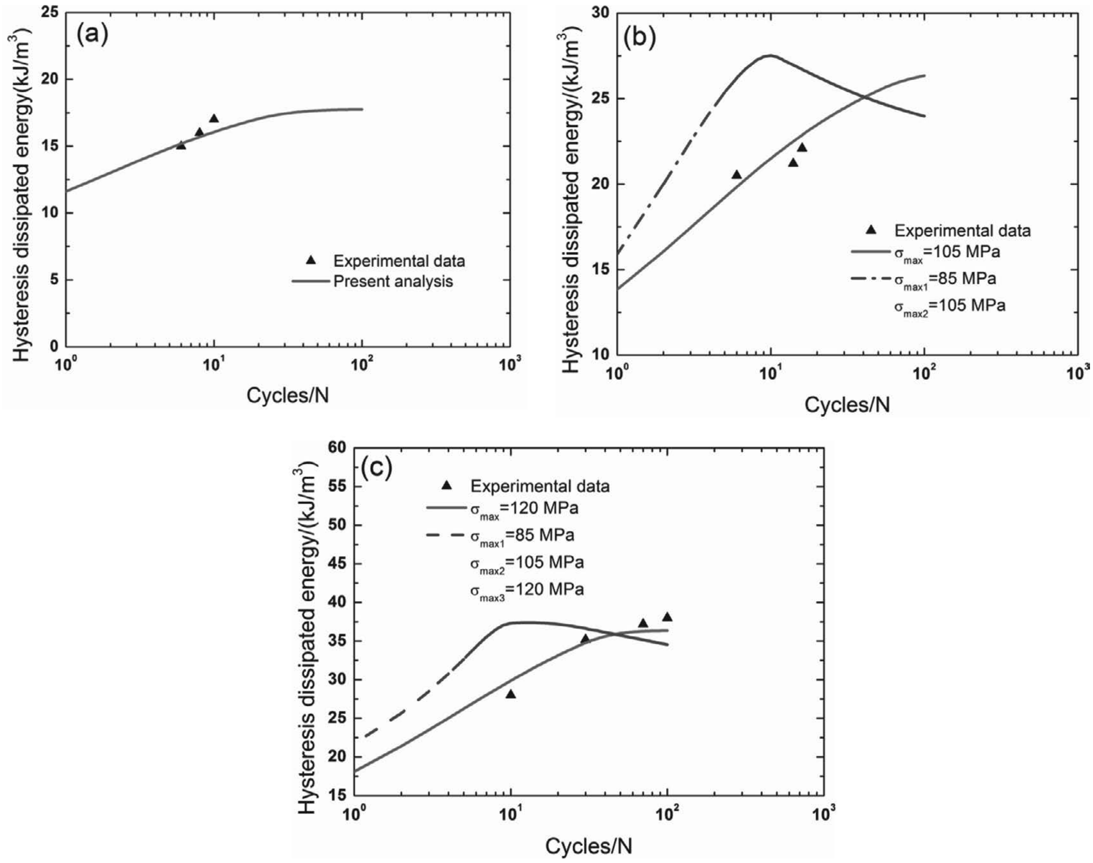

Fig. 18: The experimental in-phase thermomechanical fatigue hysteresis dissipated energy versus applied cycles curves under (a) $\sigma_{max} = 85$ MPa; (b) $\sigma_{max} = 105$ MPa, and $\sigma_{max1} = 85$ MPa/$\sigma_{max2} = 105$ MPa; and (c) $\sigma_{max} = 120$ MPa, and $\sigma_{max1} = 85$ MPa/$\sigma_{max2} = 105$ MPa/$\sigma_{max3} = 120$ MPa.

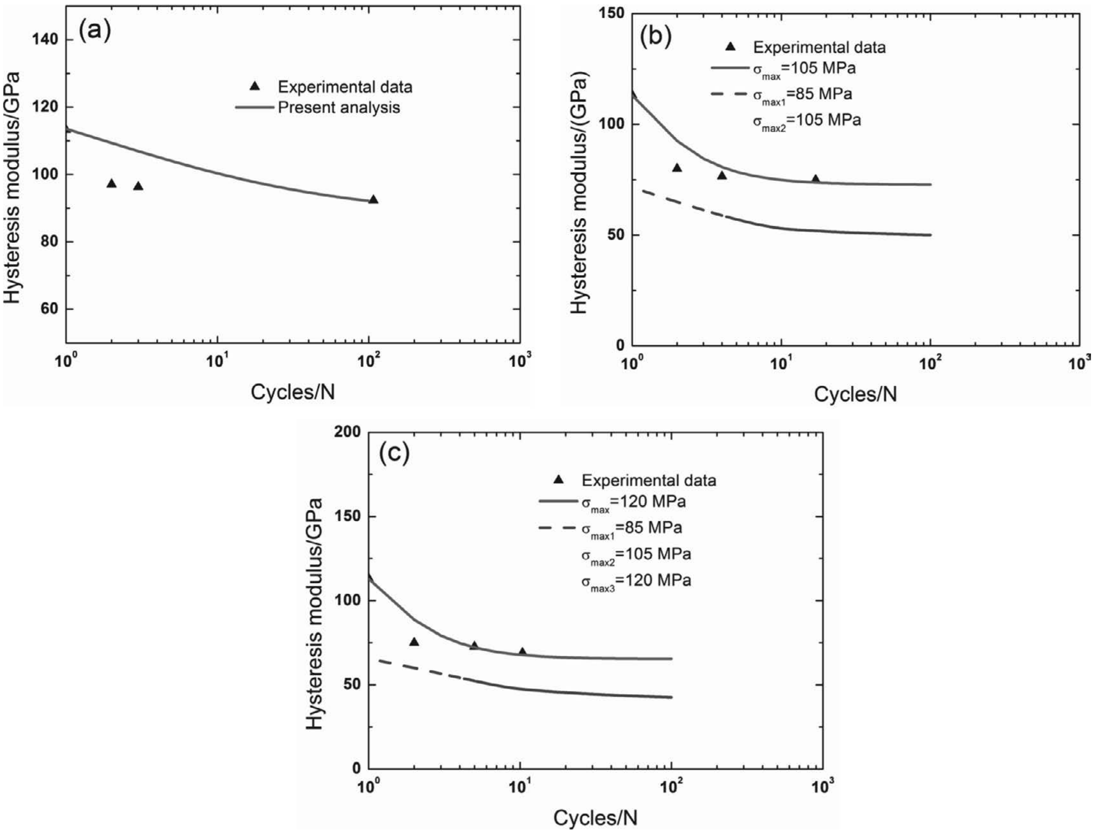

Fig. 19: The experimental in-phase thermomechanical fatigue hysteresis modulus versus applied cycles curves under (a) $\sigma_{max} = 85$ MPa; (b) $\sigma_{max} = 105$ MPa, and $\sigma_{max1} = 85$ MPa/$\sigma_{max2} = 105$ MPa; and (c) $\sigma_{max} = 120$ MPa, and $\sigma_{max1} = 85$ MPa/$\sigma_{max2} = 105$ MPa/$\sigma_{max3} = 120$ MPa.

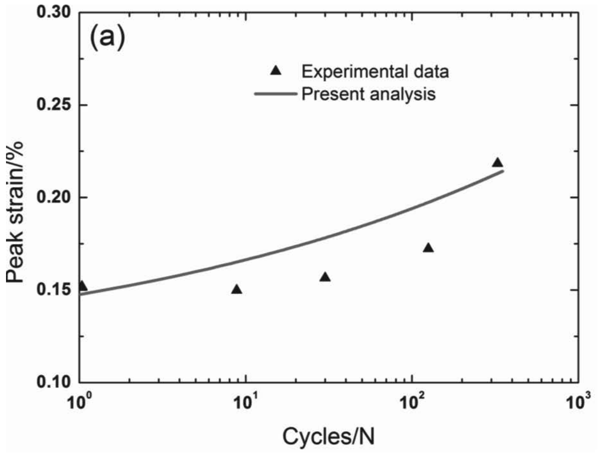

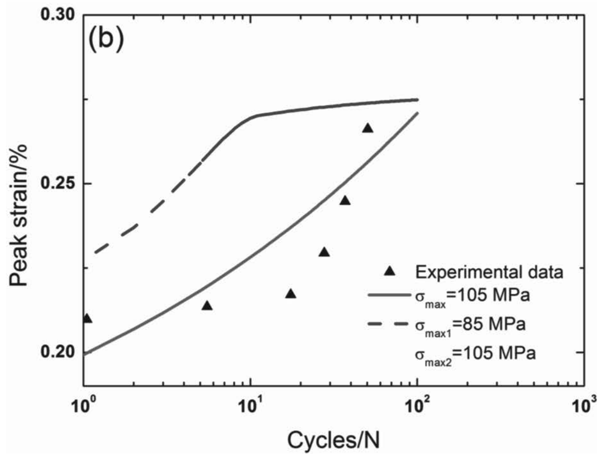

Fig. 20: The experimental in-phase thermomechanical fatigue hysteresis modulus versus applied cycles curves under (a) σ_{max} = 85 MPa; and (b) σ_{max} = 105 MPa, and σ_{max1} = 85 MPa/σ_{max2} = 105 MPa.

V. Conclusions

The synergistic effects of loading sequences and phase angles on the TMF damage evolution of SiC-fiber-reinforced CMCs have been investigated. The relationships between damage evolution, loading sequences, phase angles and micro damage states have been established. The effects of fiber volume fraction, matrix crack spacing, fiber/matrix interface debonded energy, stress ratio and thermal cyclic temperature range on the damage evolution of SiC/SiC composite for different loading sequences have been analyzed. The experimental TMF damage evolution of SiC/SiC and SiC/MAS composites subjected to different loading sequences has been predicted.

(1) Under a multiple loading sequence, the steady-state TMF hysteresis dissipated energy is the highest for the phase angle of $\theta = \pi/2$, and the lowest for the phase angle of $\theta = \pi$; the steady-state TMF hysteresis modulus is the highest for the phase angle of $\theta = \pi$, and the lowest for the phase angle of $\theta = 0$; the steady-state TMF peak strain is the highest for the phase angle of $\theta = 0$, and the lowest for the phase angle of $\theta = \pi$; the steady-state fiber/matrix interface debonding/sliding lengths are the highest for the phase angle of $\theta = 0$, and the lowest for the phase angle of $\theta = \pi$; the steady-state fiber/matrix interface debonding ratio is the highest for the phase angle of $\theta = \pi$, and the lowest for the phase angle of $\theta = 0$.

(2) With increasing fiber volume fraction, matrix crack spacing, fiber/matrix interface debonded energy, the steady-state in-phase TMF hysteresis dissipated energy and peak strain decrease; the steady-state in-phase TMF hysteresis modulus increases; the steady-state fiber/matrix interface debonding/sliding lengths and fiber/matrix interface debonding ratio decrease.

(3) With increasing stress ratio, the steady-state in-phase TMF hysteresis dissipated energy decreases; the steady-state in-phase TMF hysteresis modulus decreases; and the steady-state fiber/matrix interface sliding length decreases.

(4) With increasing thermal cyclic temperature, the steady-state in-phase TMF hysteresis dissipated energy and peak strain increase; the steady-state in-phase TMF hysteresis modulus decreases; the steady-state fiber/matrix interface debonding/sliding lengths increase; and fiber/matrix interface debonding ratio decreases.

Acknowledgements

The work reported here is supported by the Fundamental Research Funds for the Central Universities (Grant No. NS2016070).

References

1 Naslain, R.R.: SiC-matrix composites: nonbrittle ceramics for thermos-structural application, *Int. J. Appl. Ceram. Technol.*, **2**, 75 – 84, (2005).

2 Bale, H.A., Haboub, A., MacDowell, A.A., Nasiatka, J.R., Parkinson, D.Y., Cox, B.N., Marshall, D.B., Ritchie, R.O.: Real-time quantitative imaging of failure events in materials under load at temperatures above 1 600 °C, *Nat. Mater.*, **12**, 40 – 46, (2013).

3 Zok, F.W.: Ceramic-matrix composites enable revolutionary gains in turbine engine efficiency. *Am. Ceram. Soc. Bull.*, **95**, 22 – 28, (2016).

4 Levy, D.: Ceramic matrix composites take flight in LEAP jet engine. Oak Ridge National Laboratory 2017; https://www.ornl.gov/news/ceramic-matrix-composites-take-flight-leap-jet-engine

5 Cluzel, C., Baranger, E., Ladeveze, P., Mouret, A.: Mechanical behavior and lifetime modeling of self-healing ceramic-matrix composites subjected to thermomechanical loading in air, *Compos. Part A*, **40**, 976 – 984, (2009).

6 Li, L.: Modeling thermomechanical fatigue hysteresis loops of long-fiber-reinforced ceramic-matrix composites under out-of-phase cyclic loading condition, *Int. J. Fatigue*, **105**, 34 – 42, (2017).

7 Li, L.: In-phase thermomechanical fatigue damage evolution of long fiber-reinforced ceramic-matrix composites using fatigue hysteresis-based damage parameters, *Int. J. Mech. Sci.*, **140**, 189 – 199, (2018).

8 Li, L.: Modeling matrix cracking of fiber-reinforced ceramic-matrix composites under oxidation environment at elevated temperature, *Mater. Sci. Eng. A*, **87**, 110 – 119, (2017).

9 Li, L.: Damage evolution of fiber-reinforced ceramic-matrix composites under stress-rupture and cyclic loading at elevated temperature in oxidizing atmosphere, *Int. J. Mech. Sci.*, **131 – 132**, 938 – 955, (2017).

10 Li, L.: Comparisons of interface shear stress degradation rate between C/SiC and SiC/SiC ceramic-matrix composites under

cyclic fatigue loading at room and elevated temperature. *Compos. Interface*, **24**, 171 – 202, (2017).

11 Burr, A., Hild, F., Leckie, F.A.: Isochronous analysis of the behavior of ceramic-matrix composites under thermomechanical cyclic loading conditions, *Compos. Sci. Technol.*, **61**, 2231 – 2238, (2001).

12 Mei, H., Cheng, L., Zhang, L., Xu, Y.: Effect of fiber architecture on thermal cycling damage of C/SiC composites in oxidizing atmosphere, *Mater. Sci. Eng. A*, **460 – 461**, 306 – 313, (2007).

13 Foringer, M.A., Robertson, D.D., Mall, S.: A micromechanistic-based approach to fatigue life modeling of titanium-matrix composites, *Compos. Part B*, **28**, 507 – 521, (1997).

14 Gocmez, T., Awarke, A., Pischinger, S.: A new low cycle fatigue criterion for isothermal and out-of-phase thermomechanical loading, *Int. J. Fatigue*, **32**, 769 – 779, (2010).

15 Kordatos, E.Z., Aggelis, D.G., Dassios, K.G., Matikas, T.E.: *In situ* monitoring of damage evolution in glass matrix composites during cyclic loading using nondestructive techniques. *Appl. Compos. Mater.*, **20**, 961 – 973, (2013).

16 Morscher, G.N.: Modal acoustic emission of damage accumulation in a woven SiC/SiC composite. *Compos. Sci. Technol.*, **59**, 687 – 697, (1999).

17 Maillet, E., Godin, N., R¡¯Mili, M., Reynaud, P., Fantozzi, G., Lamon, J.: Real-time evaluation of energy attenuation: A novel approach to acoustic emission analysis for damage monitoring of ceramic matrix composites, *J. Eur. Ceram. Soc.*, **34**, 1673 – 1679, (2014).

18 Racle, E., Godin, N., Reynaud, P., Fantozzi, G.: Fatigue lifetime of ceramic matrix composites at intermediate temperature by acoustic emission, *Materials*, **10**, 658, (2017).

19 Simon, C., Rebillat, F., Camus, G.: Electrical resistivity monitoring of a SiC/[Si-B-C] composite under oxidizing environments, *Acta mater.*, **132**, 586 – 597, (2017).

20 Cho, C.: Relationship between frictional heating and microfailure state in a continuous fiber-reinforced ceramic matrix composite under cyclic loading, *J. Mater. Sci. Lett.*, **18**, 463 – 466, (1999).

21 Fantozzi, G., Reynaud, P.: Mechanical hysteresis in ceramic matrix composites, *Mater. Sci. Eng. A*, **521 – 522**, 18 – 23, (2009).

22 Dharan, C.K.H., Tan, T.F.: A hysteresis-based damage parameter for notched composite laminates subjected to cyclic loading, *J. Mater. Sci.*, **42**, 2204 – 2207, (2007).

23 Li, L.: A hysteresis dissipated energy-based damage parameter for life prediction of carbon fiber-reinforced ceramic-matrix composites under fatigue loading, *Compos. Part B*, **82**, 108 – 128, (2015).

24 Li, L.: Interfacial debonding and sliding of carbon fiber-reinforced ceramic-matrix composites under two stage cyclic loading, *Compos. Interfaces*, **24**, 417 – 445, (2017).

25 Li, L.: Modeling of fatigue hysteresis behavior in carbon fiber-reinforced ceramic-matrix composites under multiple loading stress levels, *J. Compos. Mater.*, **51**, 971 – 983, (2017).

26 Li, L.: Modeling of fatigue hysteresis loops in C/SiC composite under multiple loading stress levels, *Compos. Part B*, **84**, 59 – 70, (2016).

27 Fantozzi, G., Reynaud, P.: Mechanical behavior of SiC fiber-reinforced ceramic matrix composites. In V.K. Sarin (Editor-in-Chief) & L. Llanes & D. Mari (Vol. Eds.), Comprehensive Hard Materials. Elsevier, (2014).

28 Li, L.: Assessment of the interfacial properties from fatigue hysteresis loss energy in ceramic-matrix composites with different fiber preforms at room and elevated temperatures, *Mater. Sci. Eng. A*, **613**, 17 – 36, (2014).

29 Li, L.: Comparisons of interface shear stress degradation rate between C/SiC and SiC/SiC ceramic-matrix composites under cyclic fatigue loading at room and elevated temperatures, *Compos. Interfaces*, **24**, 171 – 202, (2017).

30 Reynaud, P., Douby, D., Fantozzi, G.: Effects of temperature and of oxidation on the interfacial shear stress between fibers and matrix in ceramic-matrix composites, *Acta mater.*, **46**, 2461 – 2469, (1998).

31 Li, L.: Modeling for cyclic loading/unloading hysteresis loops of carbon fiber-reinforced ceramic-matrix composites at room and elevated temperatures. Part I: theoretical analysis, *Eng. Fract. Mech.*, **164**, 117 – 136, (2016).

32 Li, L.: Modeling for cyclic loading/unloading hysteresis loops of carbon fiber-reinforced ceramic-matrix composites at room and elevated temperatures. Part II: experimental comparisons, *Eng. Fract. Mech.*, **164**, 137 – 154, (2016).

33 Evans, A.G.: Design and life prediction issues for high-temperature engineering ceramics and their composites, *Acta mater.*, **45**, 23 – 40, (1997).

34 Budiansky, B., Hutchinson, J.W., Evans, A.G.: Matrix fracture in fiber-reinforced ceramics, *J. Mech. Phys. Solids*, **34**, 167 – 189, (1986).

35 Gao, Y., Mai, Y., Cotterell, B.: Fracture of fiber-reinforced materials, *J. Appl. Math. Phys.*, **39**, 550 – 572, (1988).

36 Zhu, S., Mizuno, M., Nagano, Y., Cao, J., Kagawa, Y., Kaya, H.: Creep and fatigue behavior in an enhanced SiC/SiC composite at high temperature, *J. Am. Ceram. Soc.*, **81**, 2269 – 2277 (1998).

37 Steiner, C.D.: Fatigue behavior of a cross-ply ceramic matrix composite at elevated temperatures under tension-tension loading. Master Thesis, Air Force Institute of Technology, USA, (1994).

38 Allen, D.G., Mall, S.: Thermo-mechanical fatigue behavior of cross-ply ceramic matrix composite under tension-tension loading, *Ceram. Eng. Sci. Proc.*, **18**, 763 – 770, (1997).